Defence Technology 38 (2024) 136–154

Contents lists available at ScienceDirect

Defence Technology

journal homepage: www.keaipublishing.com/en/journals/defence-technology

Kinematic-mapping-model-guided analysis and optimization of 2-PSS&1-RR circular-rail parallel mechanism for fully steerable phased array antennas

Guodong Tan [a], Xiangfei Meng [a], Xuechao Duan [a, *], Lulu Cheng [a], Dingchao Niu [a], Shuai He [a], Dan Zhang [b]

[a] Laboratory of Electromechanical Coupling in Electronic Equipment, Xidian University, Xi'an, Shaanxi, 710071, China
[b] Department of Mechanical Engineering, The Hong Kong Polytechnic University, Kowloon, Hong Kong, 999077, China

ARTICLE INFO

Article history:
Received 10 January 2024
Received in revised form
2 February 2024
Accepted 6 March 2024
Available online 26 March 2024

Keywords:
Innovative antenna mount
Circular rail
Kinematic mapping model
Crank-slider linkage
Stiffness singularity
Backtracking

ABSTRACT

This paper presents a systematic methodology for analyzing and optimizing an innovative antenna mount designed for phased array antennas, implemented through a novel 2-PSS&1-RR circular-rail parallel mechanism. Initially, a comparative motion analysis between the 3D model of the mount and its full-scale prototype is conducted to validate effectiveness. Given the inherent complexity, a kinematic mapping model is established between the mount and the crank-slider linkage, providing a guiding framework for subsequent analysis and optimization. Guided by this model, feasible inverse and forward solutions are derived, enabling precise identification of stiffness singularities. The concept of singularity distance is thus introduced to reflect the structural stiffness of the mount. Subsequently, also guided by the mapping model, a heuristic algorithm incorporating two backtracking procedures is developed to reduce the mount's mass. Additionally, a parametric finite-element model is employed to explore the relation between singularity distance and structural stiffness. The results indicate a significant reduction (about 16%) in the antenna mount's mass through the developed algorithm, while highlighting the singularity distance as an effective stiffness indicator for this type of antenna mount.

1. Introduction

In fields such as aerospace, radio astronomy and defense, a diverse array of support equipment is required, such as deployable mechanisms for spaceborne antennas [1–8], space deployable platforms for in-orbit service stations [9,10], and various types of antenna mounts. As an important point of research, the antenna mount is a mechanism designed to support and implement the pointing of antennas of various equipment, including radar systems, radio telescopes, and more [11]. A traditional and typical antenna mount can be defined as follows: It consists of two orthogonal active axes, which are stacked one upon the other. Each of these axes is actuated by a servo motor and gearbox. This particular perpendicular-axis mount offers the benefits of a simple structure and control. Nonetheless, due to the serial nature of the two axes in terms of the mechanical arrangement, this type of mount is susceptible to the accumulation of joint errors and can become cumbersome when tasked with supporting a large-dimension antenna systems. In consideration of these drawing backs, researchers have explored the utilization of parallel mechanisms as antenna mounts, capitalizing on their notable benefits, which include high stiffness, precision, and light weight. The notable Stewart platform [12] (also called Gough hexapod) had been directly employed as antenna mounts of radio telescopes, and this attempt was first presented in the work of Dunlop et al. [13]. Many scholars have delved deeply into the relevant theories [14–19], and some practical implementations have been introduced. Examples include a 1.5 m optical telescope [20,21] and the AMiBA radio telescope [22]. Dunlop et al. also transformed the Stewart platform into a 3-degree-of-freedom (DoF) parallel mechanism known as the Kiwibot [23]. Based on the Kiwibot design, it further evolved into a novel parallel mechanism named the Canterbury tracker [24], characterized by its two DoFs and the elimination of singularities within its workspace [25]. Various lower-mobility parallel mechanisms, such as 3-RPS, 3-RSR and others, have been theoretically studied and explored for antenna mounts in published Refs. [26–30]. Xu et al. also explored the possibility of

* Corresponding author.
E-mail address: xchduan@xidian.edu.cn (X. Duan).
Peer review under responsibility of China Ordnance Society

https://doi.org/10.1016/j.dt.2024.03.001

employing hybrid parallel mechanisms for antenna mounts and verified their effectiveness by fabricating principle prototypes [31–33]. Moreover, certain spherical parallel mechanisms originally designed for applications such as camera pointing, stabilized platforms, and robotic wrists possess theoretical potential to be utilized as antenna mounts [34–40]. However, these mechanisms are relatively complex, demanding elaborate designs to achieve 0°–90° pitch motion and 0°–360° azimuth motion (i.e., fully steerable). Additionally, they are not suitable for non-centrally symmetric antennas, such as phased array antennas with rectangular fronts.

As a distinctive type of parallel mechanism, the circular-rail parallel mechanism (CRPM) possesses unlimited azimuth motion of the moving platform. Recently, scholars worldwide, particularly those from Russia, have conducted comprehensive research on this type of mechanism, covering aspects such as type synthesis, motion analysis, singularity analysis, workspace analysis, dimensional synthesis, and more [41–47]. Inspired by this kind of mechanism, in 2017, we introduced an innovative antenna mount (IAM) concept [48] for phased array antennas with rectangular fronts (also reflector antennas [49]) to replace traditional serial-type antenna mounts, aiming to achieve lightweight and simple structure, extensive motion capabilities, and absence of singularities. This IAM is a 2-PSS&1-RR CRPM, effortlessly capable of achieving pitch motion from 0 to 90° and azimuth motion from 0° to 360°. After years of effort, we have fabricated a principle prototype to verify the feasibility of this IAM concept. Initially, our research on this IAM was relatively basic and simple. For instance, the design heavily relied on iterative attempts within CAD software to determine suitable values of various structural parameters, aiming to achieve the intended workspace. We conducted only elementary research on singularities within the workspace of the IAM, lacking exploration of potential singularities beyond this area. Consequently, we were unable to evaluate their impact on the IAM's performance, particularly concerning structural stiffness. Additionally, we observed that the circular base (including the rail) of the prototype accounted for a considerable portion of its overall mass, and the high cost of manufacturing the circular gear also posed a challenge. Therefore, this research aims to propose a systematic approach to analyze and optimize the IAM. However, directly analyzing and optimizing this IAM is considerably challenging due to its complex kinematic and constraint characteristics; hence, the emphasis should be on leveraging the inherent structural features of the IAM to achieve a simplified analysis. For example, we can focus solely on the pitch motion of the IAM due to its axisymmetry at any fixed pitch angle.

Extensive simulations and experiments have revealed notable resemblances between the pitch motion of the IAM and the motion of the (planar) crank-slider linkage (CSL) [50], providing an insight into indirectly investigating the IAM's pitch motion through the study of the CSL's. This approach promises substantial simplification in the research on the IAM, due to the thorough understanding developed over the past centuries regarding the motion characteristics of the CSL. As a result, this paper successfully establishes a kinematic mapping model between the CSL and the IAM to construct an analytical framework. Within this framework, various challenging analysis problems are addressed, encompassing the utilization of the CSL's multi-solution nature to determine feasible forward and inverse solutions to the IAM, determining singular configurations within the IAM through the CSL's dead-point and boundary singularities, and further identifying singularity types through visual graphical methods. Building upon the aforementioned work, the concept of singularity distance is introduced as a means to evaluate how singularities impact the stiffness of the IAM within its tasked workspace. Following this, utilizing the framework and integrating the backtracking method, an efficient optimization algorithm is developed to reduce the mass of the IAM.

The subsequent layout of this paper encompasses the following sections. Section 2 elaborates on the operational principles of the IAM, validating the feasibility of the proposed concept through a comparative analysis between the 3D model and the principle prototype. Section 3 establishes a kinematic mapping model that interrelates the IAM and the CSL. Section 4 determines the feasible forward and inverse solutions to the IAM, guided by the mapping model. Section 5 locates and further identifies the singularities inherent to the IAM, using the mapping model. Section 6 focuses on designing an efficient optimization algorithm for reducing the IAM's mass, guided by the mapping model. Section 7 presents the optimization results and conducts an in-depth discussion. Finally, Section 8 culminates by presenting several pivotal conclusions derived from the research.

2. Innovative antenna mount

Our previous work in Ref. [48] had performed a brief introduction of the 2-PSS&1-RR circular-rail parallel mechanism consisting of the IAM, and established a simple 3D model to verify the effectiveness of the IAM by numerical simulation. This section will carry out a more in-depth investigation by the comparison between the fabricated principle prototype and the 3D model to verify the effectiveness further.

2.1. Operational principle

Presented in Fig. 1(a) is the schematic diagram of the IAM for phased array antennas, in which its antenna front is connected to the column through a revolute joint (pitch axis), followed by another revolute joint (azimuth axis) in series. On a circular rail with a radius of R, there are two actuators, labeled A_1 and A_2, that can slide along the rail. The upper ends of two equal-length rods (limbs), P_1A_1 and P_2A_2, are connected to the rotation axis P_1P_2 through 3-DoF compound joints (equivalent to the ball joint) and the lower ends are connected to points A_1 and A_2 through another 3-DoF compound joints, as shown in Figs. 1(a) and 1(c). The rotation axis P_1P_2 is parallel to the pitch axis at the top of the column, with a height difference of d. The positions of points P_1 and P_2 are presented in Fig. 1(b).

In the established global coordinate system O-XYZ, the rail plane is defined as the XOY plane with its center at the origin O. The central axis of the column is aligned with the Z-axis. The projection (B) of the midpoint P of the line segment P_1P_2 onto the XOY plane lies in the X-axis. The orientation of the Y–axis is determined in accordance with the right-hand rule. A local coordinate system, denoted as o-xyz (colored in blue), is affixed to the front, aligning its axes in parallel with those of O-XYZ when the front is in the position depicted in Fig. 1(a).

When the two actuators asynchronously rotate about the Z-axis on their respective half rails, the pitch motion of the front is achieved, and the pitch angle is denoted as φ. When they synchronously rotate about the Z-axis on the rail, the front achieves the azimuth motion. The azimuth angle is denoted as γ, as shown in the top view of Fig. 1(a). The angular position of the actuators is denoted as θ. If $\theta = \theta_z$, then $\varphi = 0$, and hence the front is in the zenith position, colored in red. If $\theta = \theta_h$, then $\varphi = 90°$, and thus the front is in the horizon position, colored in blue. In this way, continuous increase of θ from θ_z to θ_h and the synchronous rotation of the two actuators by 360° along the rail, supplies the tasked workspace (TWS), as follows

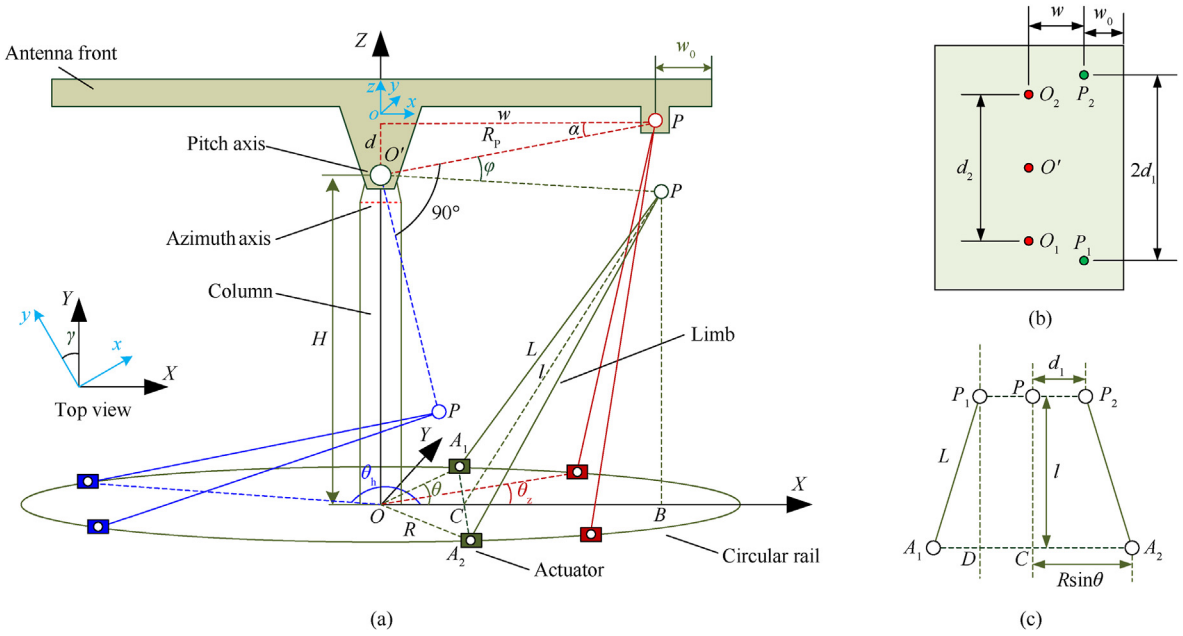

Fig. 1. Schematic diagram of innovative antenna mount (IAM): (a) Front view of antenna mount; (b) Bottom view of antenna front; (c) Side view of limbs. Point P represents the midpoint of P_1 and P_2, as shown in Fig. 1(c). While point O' represents the midpoint of O_1 and O_2, as shown in Fig. 1(b).

$$\mathrm{TWS} \triangleq \{(\varphi, \gamma) | \varphi \in [0, 90^\circ], \gamma \in [0, 360^\circ]\} \quad (1)$$

which is necessary to most steerable antennas. In addition, the maximum workspace that the front can attain is named as the maximum workspace (MWS), and it is obvious that the TWS is contained in the MWS. The TWS can be further partitioned into a 0°–90° pitch-angle space (PAS) and a 0°–360° azimuth angle space (AAS).

2.2. 3D model and prototype

The implementation of the IAM concept in Fig. 1, i.e. the 3D model, is presented in Fig. 2(a). According to Fig. 2(a), the IAM is a parallel mechanism composed of 3 kinematic chains, a central chain composed of two revolute joints, and two identical side chains composed of two compound joints and a prismatic joint. The compound joint is equivalent to a ball joint. As a result, the IAM can be considered as a 2-PSS&1-RR parallel mechanism (The IAM can also be viewed as a 2-RSS&1-RR parallel mechanism since the circular moving pair is equivalent to a revolute joint). In Ref. [48], we had proven that within the TWS the mechanism has two DoFs: a rotation about the column axis (azimuth motion) and a rotation about the pitch axis (pitch motion).

To verify the effectiveness of the proposed IAM, we have manufactured a full-scale prototype of the 3D model, as shown in Fig. 2(b). The comparisons between the motion of the 3D model and the prototype, including pitch and azimuth motions, are shown in Figs. 3 and 4, respectively. It can be seen from these figures that the motions of the 3D model and the prototype agree well, and the experimental results of the prototype affirm that the IAM indeed

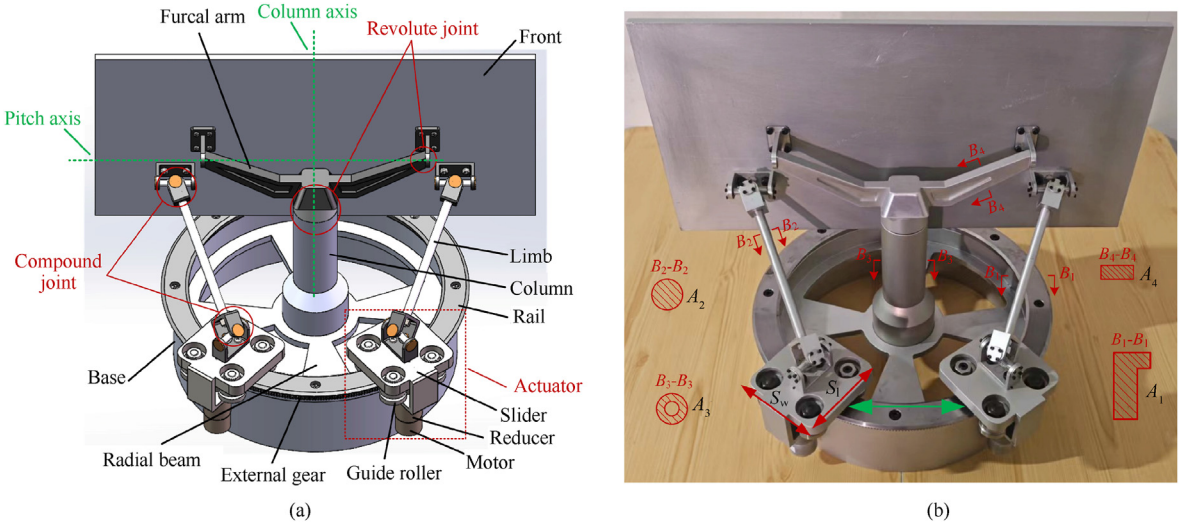

Fig. 2. Innovative antenna mount (front in horizon position): (a) 3D model; (b) Full-scale prototype.

possesses two DoFs—the pitch and azimuth motions— within the TWS.

The values of the relevant structural parameters, including lengths, areas, and masses, presented in Figs. 1 and 2 are listed out in Table 1. It can be seen from Table 1 that the mass (M_b) of the base (including the rail) accounts for nearly half of the total mass (M) of the IAM prototype. On the other hand, when the antenna front is in the horizon position (the extreme position), the distance between the two actuators remains substantial, as indicated by the bidirectional green arrow in Fig. 2(b). This phenomenon suggests that the circular rail is not fully utilized. Therefore, there is potential to minimize the radius of the circular rail to further reduce the mass of the IAM. However, an inappropriate reduction in the rail radius may lead to the IAM's inability to meet some necessary requirements such as the TWS, collision-free of actuators and so on. Therefore, a detailed study of the kinematics of the IAM is necessary to elucidate the relation between the rail radius and these requirements. Given the complexities of the IAM—a 2-PSS&1-RR circular rail parallel mechanism—this study aims to heuristically establish a kinematic mapping model between the CSL and the IAM, simplifying the analysis process. Utilizing this model and analysis outcomes, a heuristic approach will be employed to optimize the IAM, aiming to achieve mass reduction.

3. Kinematic mapping model

Due to the intricate nature of the IAM, this section introduces a kinematic analysis model from the similarity between the IAM and the CSL, aiming to solve subsequent problems of both forward and inverse kinematics, singularity analysis, and mechanism optimization in a simpler way. This model consisting of a mapping from the kinematic characteristics of the CSL to those of the IAM, leading to a considerable simplification in the kinematic analysis process. In view of the axisymmetry of the azimuth motion, the below analysis focuses solely on the pitch motion.

3.1. Mapping relation between innovative antenna mount and crank-slider linkage

According to the characteristics of the pitch motion of the IAM in Fig. 1, it is considerably like the motion that a CSL possesses. Hence, in this case, the IAM can be mapped as a CSL for the convenience of discussion, as shown in Fig. 5. The antenna front is equivalent to the crank of the CSL, the limb is equivalent to the coupler, the actuator is equivalent to the slider, and the rail is equivalent to the slide. If the antenna front undergoes pitch motion driven by the limbs, it is equivalent to the crank undergoing pitch motion driven by the coupler. If R is infinitely large, the circular rail will transform into a straight line, and thus the sliding of the actuator on the rail becomes identical to the linear sliding of the slider on the CSL slide. Therefore, this mapping appears highly reasonable. In fact, our extensive simulations and experiments have demonstrated the correctness and rationality of the mapping.

On the other hand, the motion range of the actuator is limited. As shown in Fig. 6(a), the two actuators are constrained within an interval I_b in order to avoid the collision between them. According to the geometric relation in Fig. 6(b), we have

$$I_b = [\theta_b, \pi - \theta_b] \tag{2}$$

where, $\theta_b = \arctan((S_w/2)/(R - S_l/2)) = \arctan(S_w/(2R - S_l))$

Therefore, as illustrated in Fig. 5(a), there is a boundary on the rail, circled by the red dashed line. In order to map this boundary into the CSL, a barrier can be artificially added into the CSL. As a result, the IAM is mapped into a crank-slider linkage with barriers (CSL-B), and the mapping model in Fig. 5 is named as the kinematic mapping model (KMM). The mapping details between the IAM and CSL-B is summarized in Table 2. Thereinto, the concept of singularity distance (D_s and d_s) in this table will be introduced in Section 5.

As a result, the usage of the KMM is summarized in Fig. 7. If we intend to conduct particular research on the IAM, we can carry out the corresponding research on the CSL-B, according to the KMM.

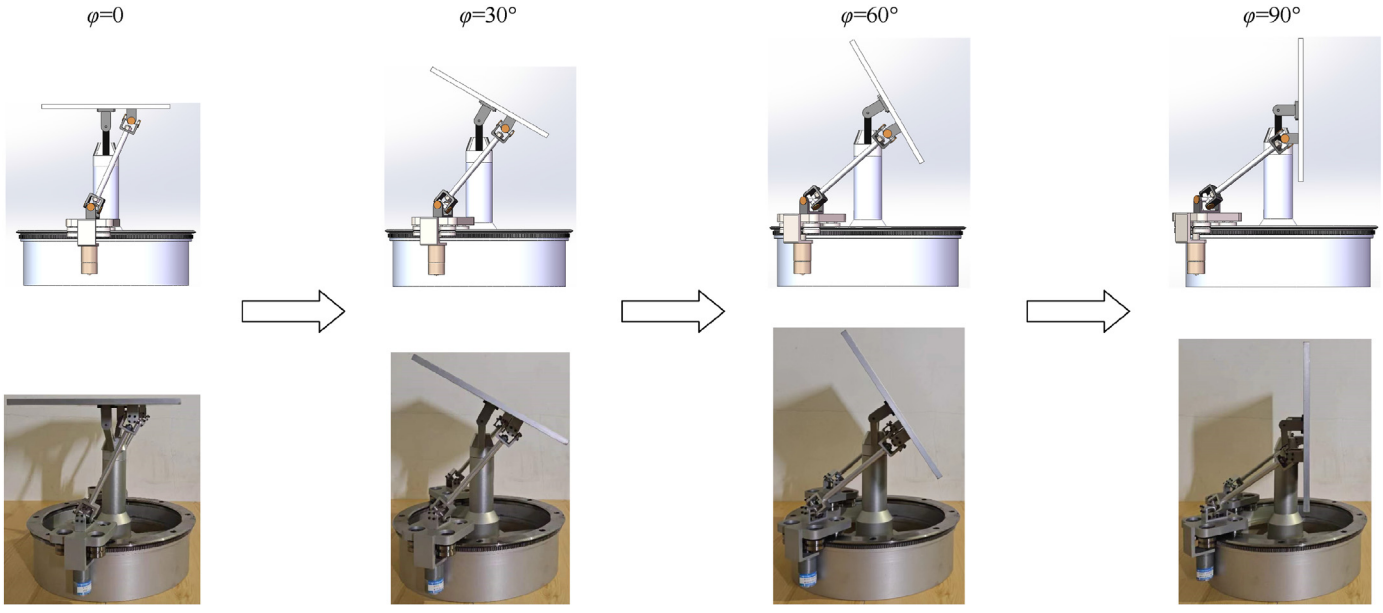

Fig. 3. Comparison of pitch motion ($\gamma = 0°$).

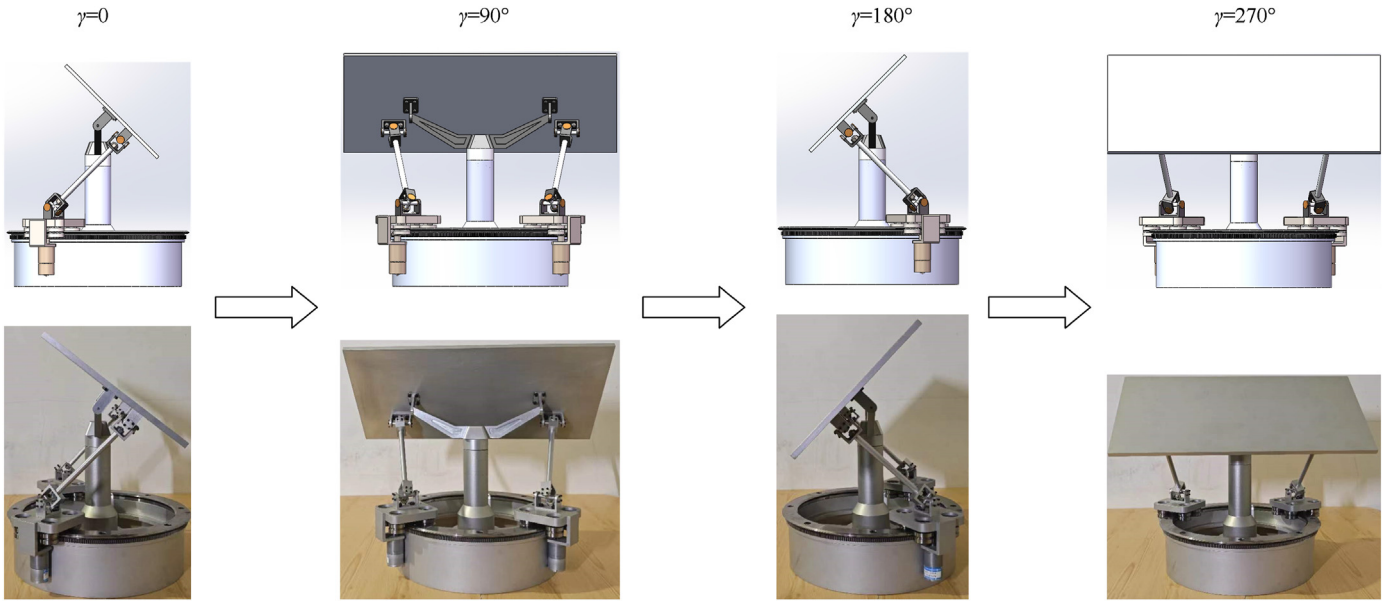

Fig. 4. Comparison of azimuth motion ($\varphi = 45°$).

Table 1
Structural parameters of prototype.

Parameter	Length/mm									
	d	d_1	d_2	H	R	L	w	w_0	S_l	S_w
Value	9.4	127	204	124.80	125.61	147.11	39.72	60	75	75
Parameter	Area/mm^2				Mass/kg					
	A_1	A_2	A_3	A_4	M	M_b	M_c	M_l		
Value	928.9	50.27	725.71	130.38	6.111	3.142	0.323	0.017		

*M represents the total mass of the IAM prototype and M_b represents the total mass of the base and rail. The total mass of the base, limbs and the column are denoted as M_{blc}=M_b+2M_l+M_c=3.499 kg.

Conversely, employing the obtained research results, relevant methods or techniques, and appropriate reasoning, the corresponding research on the IAM is carried out according to the KMM. This research is more in-depth compared to the initial one on the CSL-B. Sections 4 to 8 will demonstrate the practical application of the KMM (In all figures of Sections 4 and 5, the "barrier" in Fig. 5(b) will not be involved, so it is not drawn for simplicity.).

4. Kinematic analysis

Simulated and experimental results indicate that the IAM possesses multiple solutions to both forward and inverse kinematics, making it challenging to determine the feasible solutions. Hence, this section employs the KMM proposed in Section 3 to identify the feasible solutions, coupled with the singularity analysis in Section 5 to ensure the absence of singularities within these feasible solutions.

4.1. Inverse kinematics

Referring to the geometric relation in Figs. 1(a) and 1(c), the following relations are obtained:

$$\begin{cases} \overline{PB}^2 + \overline{BC}^2 = l^2 \\ l^2 + \overline{A_1D}^2 = L^2 \end{cases} \tag{3}$$

where, $\overline{PB} = H - R_p\sin(\varphi - \alpha)$, $\overline{BC} = R_p\cos(\varphi - \alpha) - R\cos\theta$, $\overline{A_1D} = R\sin\theta - d_1, R_p = \sqrt{w^2 + d^2}$ and $\alpha = \arctan(d/w)$.

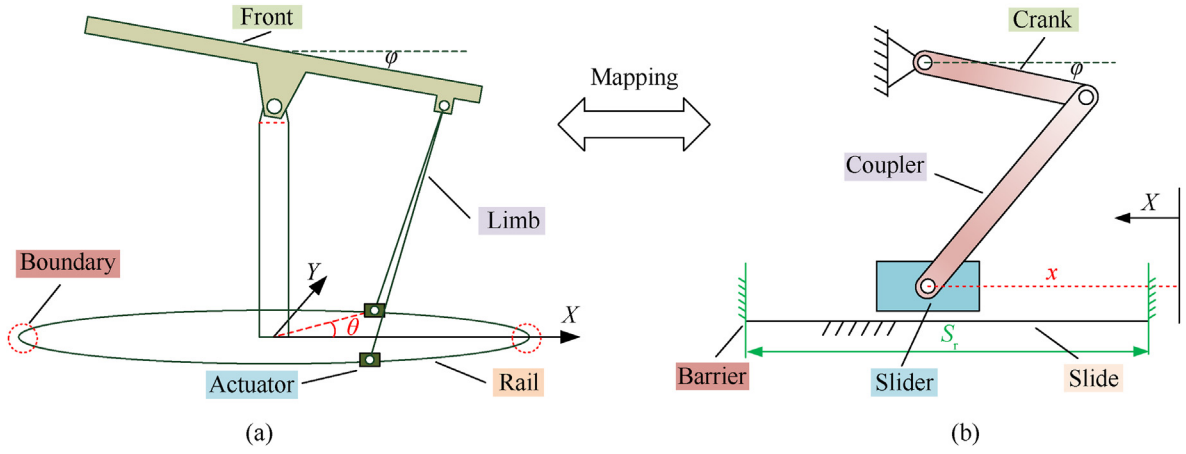

Fig. 5. Kinematic mapping model: (a) Innovative antenna mount; (b) Crank-slider linkage with barriers.

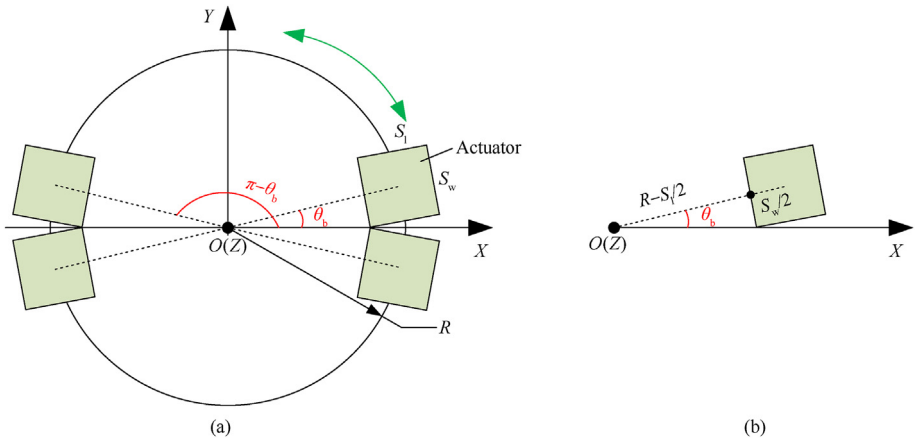

Fig. 6. Boundary interval.

Table 2
Mapping details between IAM and CSL-B.

IAM	Front	Limbs	Actuators	Rail	Motion range l_b	Angular position θ	Pitch angle φ	Singularity distance D_s
CSL-B	Crank	coupler	Slider	Slide	Restricted stroke S_r	position x	Pitch angle φ	Singularity distance d

*The concept of singularity distance will be introduced in Section 5.

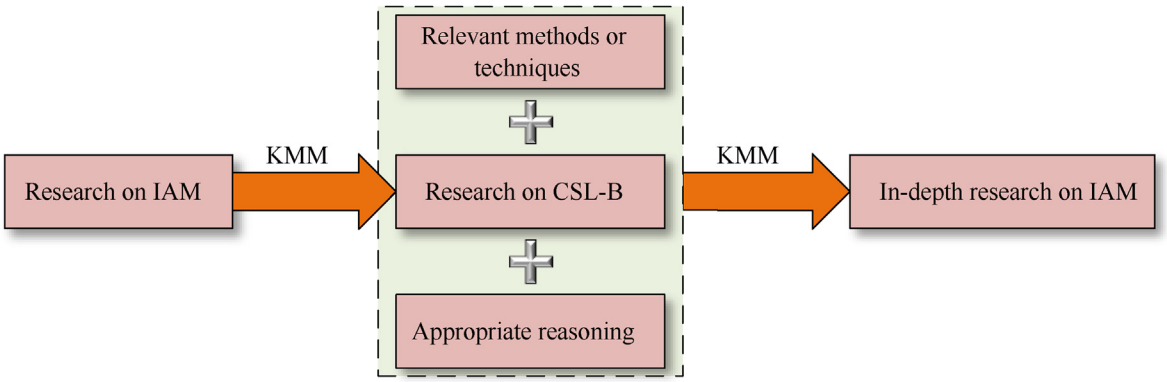

Fig. 7. Usage of kinematic mapping model.

Substituting the relevant terms into Eq. (3) yields.

$$[H-R_p\sin(\varphi-\alpha)]^2+[R_p\cos(\varphi-\alpha)-R\cos\theta]^2+(R\sin\theta-d_1)^2=L^2 \tag{4}$$

For the inverse kinematics, expanding and rearranging the equation above gives

$$d_1\sin\theta+R_p\cos(\varphi-\alpha)\cos\theta=\frac{d_1^2+H^2+R_p^2+R^2-L^2-2HR_p\sin(\varphi-\alpha)}{2R} \tag{5}$$

and Eq. (5) is denoted as

$$a_1\sin\theta+b_1\cos\theta=B_1 \tag{6}$$

where, $a_1=d_1$, $b_1=R_p\cos(\varphi-\alpha)$ and $B_1=\left(d_1^2+H^2+R_p^2+R^2-L^2-2HR_p\sin(\varphi-\alpha)\right)/(2R)$. Hence, Eq. (6) can be transformed into as follows

$$A_1\cos(\theta-\omega_1)=B_1 \tag{7}$$

where $A_1=\sqrt{a_1^2+b_1^2}$ and $\omega_1=\arccos(b_1/A_1)$. Eq. (7) has two solutions, which can be illustrated by the CSL-B in Fig. 8. By sampling at $\varphi=0°, 45°, 90°$, it is found that there exist two inverse solutions, i.e., the positions of the slider, symmetric about the branch line. In order to distinguish these two kinds of inverse solution, the sliders are colored with blue (first solution) and green (second solution), respectively. In the case of $\varphi=0°$, if the blue

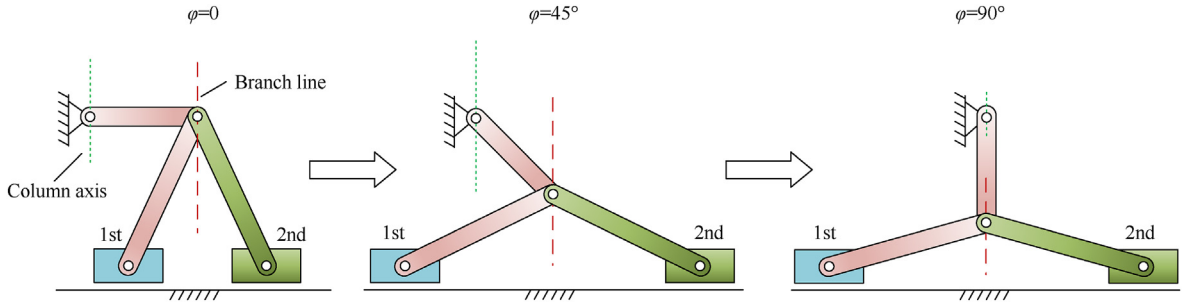

Fig. 8. Two kinds of inverse solution of CSL-B. The red dashed line is the branch line which divides two groups of different inverse solutions.

slider continuously moves to the left the crank will continuously rotate from $\varphi = 0°$ to $\varphi = 90°$. Hence, the pitch motion of the front traversing the TWS is achieved, namely, i.e., the first solution is feasible.

As for the second solution, it can be proved that the solution is unfeasible. For example, if the slider at $\varphi = 0°$ moves to the left (without crossing the branch line), the crank will rotate counter-clockwise and is out of the TWS, as shown in Fig. 9(a). However, if the slider moves to the right, the crank is in the TWS constantly. In this case, the crank and coupler will be eventually co-linear, which

$$H\sin(\varphi-\alpha)+R\cos\theta\cos(\varphi-\alpha)=\frac{d_1^2+H^2+R_P^2+R^2-L^2-2Rd_1\sin\theta}{2R_P} \tag{12}$$

indicates the maximum pitch angle is φ_m, less than 90°, as shown in Fig. 9(b). To sum up, the feasible solution to the CSL-B is only the first one. According to the KMM, we can find the similar phenomena presented in Figs. 8 and 9 for the IAM.

The two solutions of Eq. (7), denoted as θ_1^* and θ_2^*, can be formulated as follows

$$\begin{cases}\theta_1^*=-\arccos\dfrac{B_1}{A_1}+\omega_1\\ \theta_2^*=\arccos\dfrac{B_1}{A_1}+\omega_1\end{cases} \tag{8}$$

According to Fig. 8, the feasible solution of the CLS-B is on the left side of the branch line. Hence, it is inferred from the KMM that the feasible solution to the IAM is greater. Since

$$\theta_2^*-\theta_1^*=2\arccos\frac{B_1}{A_1}>0 \tag{9}$$

the feasible solution is θ_2^*. As a result, the explicit expression of the inverse solution θ_2^*, redenoted as θ, is

$$\theta=\arccos\frac{d_1^2+H^2+R_P^2+R^2-L^2-2HR_P\sin(\varphi-\alpha)}{2R\sqrt{d_1^2+[R_P\cos(\varphi-\alpha)]^2}}+\arccos\frac{R_P\cos(\varphi-\alpha)}{\sqrt{d_1^2+[R_P\cos(\varphi-\alpha)]^2}} \tag{10}$$

In this way, the angular position interval I_a of the actuator corresponding to the 0°–90° pitch angles of the front can be formulated as follows

$$I_a=[\theta_z,\theta_h]=[\theta(0°),\theta(90°)] \tag{11}$$

4.2. Forward kinematics

Regarding the forward kinematics, Eq. (5) can be rearranged into the following expression

Similarly, the equation above is denoted as the following form

$$a_2\sin(\varphi-\alpha)+b_2\cos(\varphi-\alpha)=B_2 \tag{13}$$

where $a_2=H, b_2=R\cos\theta$ and $B_2=\left(d_1^2+H^2+R_P^2+R^2-L^2-2Rd_1\sin\theta\right)/(2R_P)$. Consequently, Eq. (13) can be transformed into as follows

$$A_2\cos(\varphi-\alpha-\omega_2)=B_2 \tag{14}$$

where $A_2=\sqrt{a_2^2+b_2^2}, \omega_2=\arccos\frac{b_2}{A_2}$. Eq. (14) also has two solutions denoted as φ_1^* and φ_2^*, respectively, as illustrated in Fig. 10. Three slider positions are sampled, and two circles are constructed with O_1 and O_2 as their centers, intersecting at two points. Connecting these points with O_1 and O_2 yields two configurations of the CSL-B colored with red and green, respectively. These two configurations each have a crank located at a different position, corresponding to two forward solutions φ_1^* and φ_2^*, respectively. If the slider is in the initial position, and it continuously moves to the left-spanning the initial, middle, and end positions-φ_1^* will gradually increase from 0° to 90°, hence it is a feasible solution. Simultaneously, φ_2^* will also gradually increase, but φ_2^* is greater than 90° and the crank is on the left side of the column axis. This phenomenon indicates that the crank is interfering with the column, according to Fig. 1. Hence, φ_2^* is not a feasible solution. Referring into Fig. 10, it can be found that $\varphi_1^*<\varphi_2^*$.

The two solutions (φ_1^* and φ_2^*) of Eq. (14) are given by

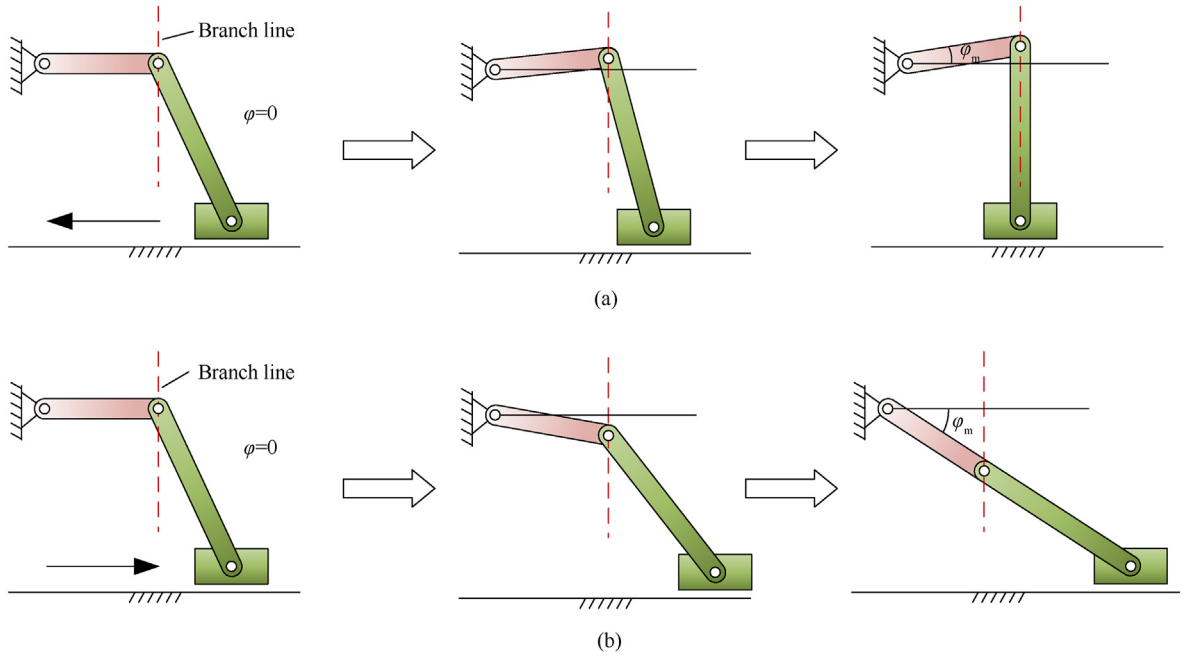

Fig. 9. Unfeasible solution: (a) Left motion; (b) Right motion.

$$\begin{cases} \varphi_1^* = -\arccos\dfrac{B_2}{A_2} + \alpha + \omega_2 \\ \varphi_2^* = \arccos\dfrac{B_2}{A_2} + \alpha + \omega_2 \end{cases} \tag{15}$$

and

$$\varphi_2^* - \varphi_1^* = 2\arccos\frac{B_2}{A_2} > 0 \tag{16}$$

Therefore, the desired forward solution to the IAM is φ_1^* according to the KMM. It is redenoted as φ, and its explicit expression is as follows

$$\varphi = -\arccos\frac{d_1^2 + H^2 + R_P^2 + R^2 - L^2 - 2Rd_1\sin\theta}{2R_P\sqrt{H^2 + (R\cos\theta)^2}} + \alpha + \arccos\frac{R\cos\theta}{\sqrt{H^2 + (R\cos\theta)^2}} \tag{17}$$

In summary, only the configurations of the CSL-B where the crank and coupler colored in red represent the feasible solutions to the IAM, including both inverse solution and forward solution. Hence below, the CSL-B only draws this kind of configuration whose crank and coupler colored in red.

5. Singularity analysis

Singular configurations are particular poses of the end-effector, for which parallel mechanisms lose their inherent rigidity, and in which the end-effector will have uncontrollable DoFs. The most common method for singularity analysis involves assessing the conditional number (denoted as Cond(•)) of the Jacobian matrix [51]. In our initial research [48], we utilized this approach to demonstrate the absence of singularities within the TWS. However, we did not account for the impact of the potential singularities (outside the TWS) on the motion performance within the TWS. In this section, we will employ the KMM to identify singular configurations of the IAM and adopt the visual graphical approach to recognize their types.

5.1. Stiffness singularity

The configuration of the dead-point singularity [52] of the CSL-B is shown in Fig. 11(a), where the axis of the coupler is perpendicular to the slide. As a result, the coupler is unable to supply any component force along the motion direction of the slider. Inspired

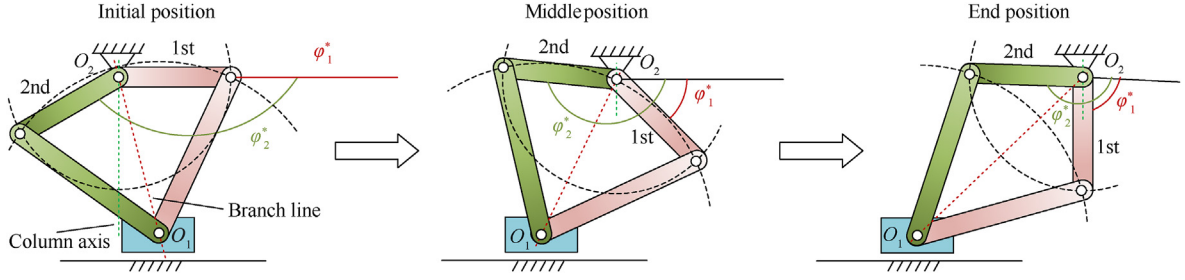

Fig. 10. Forward solutions: The light red links correspond the first forward solution and the light green links correspond the second solution.

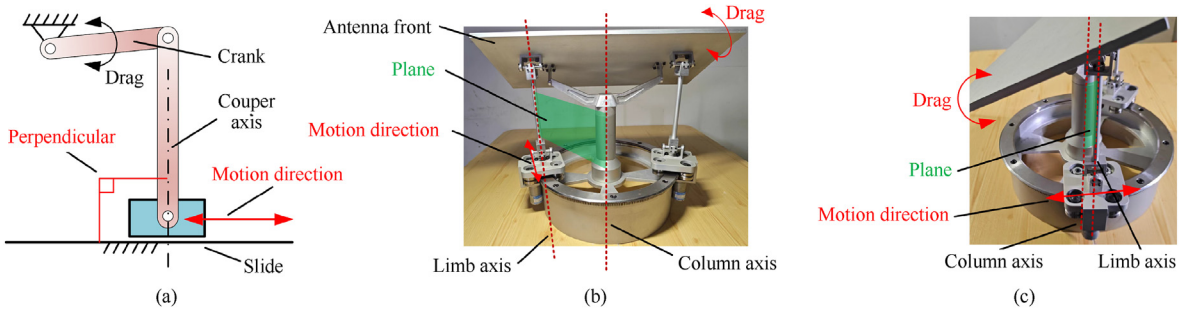

Fig. 11. Phenomenon of dead-point singularity: (a) Dead-point singularity of CSL-B; (b) Front view of singular configuration; (c) Side view of singular configuration.

by this phenomenon and according to the KMM, it is found that the similar singularity occurs outside the TWS of the IAM if the limb axis and the column axis are coplanar, as shown in Figs. 11(b) and 11(c). In this case, the plane (colored in green) determined by the column axis and limb axis is perpendicular to the motion direction of the actuator, This fact implies that the force exerted by the limb is entirely confined within this plane, with no any component force available to drive the actuator. Hence, if we manually drag the antenna front as the manner in Figs. 11(b) and 11(c), the actuators will not move. This phenomenon indicates that this configuration of the IAM has the similar singular characteristics as those of the CSL-B (dead-point singularity).

However, the dead-point singularity of the CSL-B occurs only when the crank is used as the driver while the IAM's driver is not the antenna front but the two actuators. Therefore, the visual graphical approach in Refs. [53–55] is employed to further analyze this singular configuration and identify its type, the analysis procedure is presented in Fig. 12. Fig. 12(a) gives the freedom line pattern of branch chains, and hence the constraint line pattern of the antenna front (moving platform) can be given by the generalized Blanding rules (GBRs) [53–55], as shown in Fig. 12(b). Further application of the GBRs yields the freedom line pattern of the antenna front, as shown in Fig. 12(c). It can be seen from Fig. 12(c) that the antenna front has a DoF rotating about the Z-axis, indicating in this configuration the stiffness of the IAM is zero (the two actuators have been locked). According to the definition and classification method outlined in Ref. [56], we can further demonstrate that this singularity belongs to the category of input transmission singularity. Taking into account the zero stiffness characteristics exhibited in this configuration, this singularity is deliberately named as stiffness singularity.

As illustrated in Fig. 13, if dragging the front about the Z-axis by hand, the antenna front will rotate about the Z-axis, while the two actuators remain locked. This experimental phenomenon indicates that, in this configuration, the two kinematic chains completely lose their constraint effect on the front, which is in complete agreement with the theoretical analysis results in Fig. 12. In the vicinity of the stiffness singularity, the overall performance of the mechanism (such as stiffness and precision) deteriorates [57], leading to uncontrollable behavior. Therefore, the TWS of the IAM must maintain a considerable distance from this stiffness singularity.

Next, we utilize the screw theory to find the theoretical value of the actuator position where the stiffness singularity occurs. Referring to Fig. 1, the screw of the column axis is

$$\$_c = [0, 0, 1; 0, 0, 0]^{\mathrm{T}} \tag{18}$$

The coordinates of $\overrightarrow{OA_1}$ and $\overrightarrow{A_1P}$ are as follows

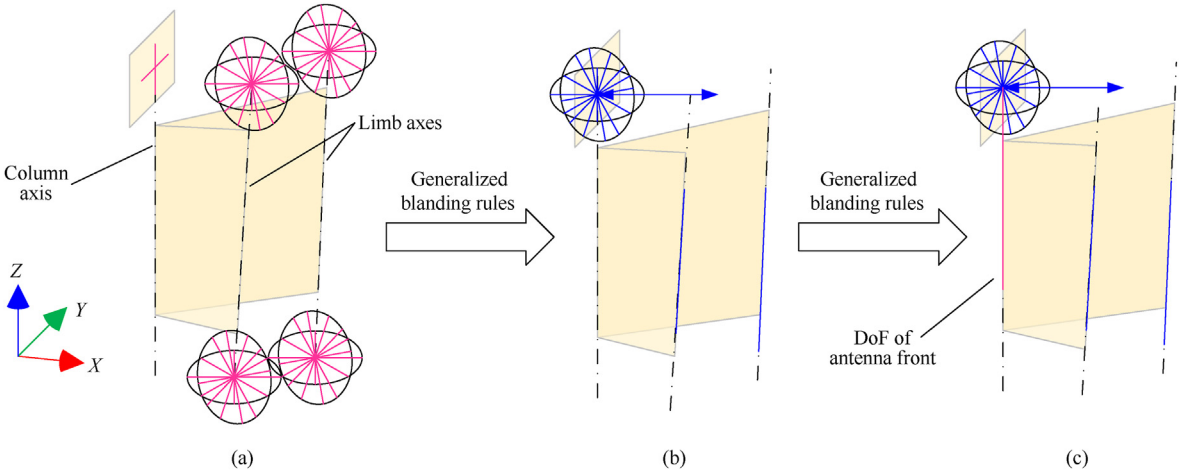

Fig. 12. DoF analysis of stiffness-singular configuration by graphical approach: (a) Freedom line pattern of branch chains; (b) Constraint line pattern of antenna front; (c) DoF of antenna front. In above figure, the pink lines and arrow represent DoFs as well as the blue the constraints.

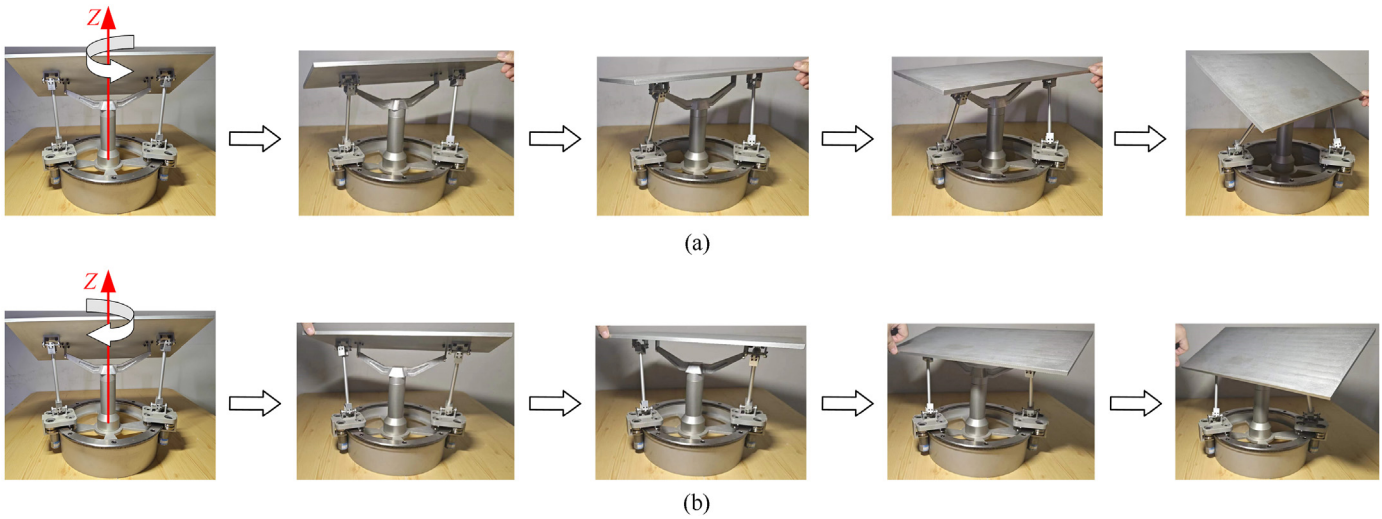

Fig. 13. Demonstration of stiffness singularity: (a) Rotation about +*Z* axis; (b) Rotation about -*Z* axis.

$$\begin{aligned}\overrightarrow{OA_1} &= (R\cos\theta, R\sin\theta, 0)^{\mathrm{T}},\ \overrightarrow{A_1P}\\ &= \{R_{\mathrm{P}}\cos(\varphi-\alpha), d_1, H - R_{\mathrm{P}}\sin(\varphi-\alpha)\}^{\mathrm{T}}\\ &\quad - (R\cos\theta, R\sin\theta, 0)^{\mathrm{T}}\\ &= \{R_{\mathrm{P}}\cos(\varphi-\alpha) - R\cos\theta, d_1 - R\sin\theta, H - R_{\mathrm{P}}\sin(\varphi-\alpha)\}^{\mathrm{T}}\end{aligned} \tag{19}$$

Hence, the screw of the limb axis is

$$\begin{aligned}\$_{\mathrm{l}} &= \left(\overrightarrow{A_1P}, \overrightarrow{OA_1}\times\overrightarrow{A_1P}\right)^{\mathrm{T}}\\ &= \{R_{\mathrm{P}}\cos(\varphi-\alpha) - R\cos\theta, d_1 - R\sin\theta, H - R_{\mathrm{P}}\sin(\varphi\\ &\quad -\alpha);\ R\sin\theta[H + R_{\mathrm{P}}\sin(\alpha-\varphi)], -R\cos\theta[H + R_{\mathrm{P}}\sin(\alpha\\ &\quad -\varphi)], R[d_1\cos\theta - R_{\mathrm{P}}\cos(\alpha-\varphi)\sin\theta]\}^{\mathrm{T}}\end{aligned} \tag{20}$$

Due to the cop1anarity of the limb axis and the column axis, hence

$$\$_{\mathrm{c}}\circ\$_{\mathrm{l}} = R[d_1\cos\theta - R_{\mathrm{P}}\cos(\alpha-\varphi)\sin\theta] = 0 \tag{21}$$

where symbol "∘" re presents the reciproca1 product [52]. Furthermore, substituting Eq. (17) into Eq. (21) and simplifying the resulting equation, we arrive at

$$\begin{cases} d_1\cos\theta - R_{\mathrm{P}}\cos(\alpha-\varphi)\sin\theta = 0\\ 0^\circ < \theta < 180^\circ\end{cases} \tag{22}$$

which is a trigonometric equation with respect to θ in interval (0°, 180°), and hence is a typical constraint satisfaction problem (CSP). After solving the equation in Eq. (22), its solution is denoted as θ_{s}, as shown in Table 3. In this position the conditional number of the Jacobian matrix $\boldsymbol{J}$ (see Ref. [48]) is about 7.2×10^6, as shown in Table 3. This result indicates that there occurs the singularity if the actuator is in the position θ_{s}, which is totally in agreement with our analysis in Fig. 12.

5.2. Boundary singularity

As shown in Fig. 14(a), when the coupler axis is co-linear with the crank axis, the boundary singularity occurs. Regardless of the force applied to drag the slider, the CSL-B will remain motionless. this phenomenon is attributed to the transmission angle of CSL-B being 0, causing the inability of the coupler to provide any torque for rotating the crank. the IAM theoretically exhibits a similar phenomenon; if the limb axis is co-planar with the pitch axis, this kind of singularity will occur. However, experimental observations on the prototype have revealed that interference occurs within the compound joint even before the prototype configuration reaches the boundary singularity, as illustrated in Figs. 14(b) and14(c). The interference prevents the prototype from reaching the boundary singularity, suggesting that the IAM exhibits a boundary singularity outside the TWS solely in theory.

Referring to Fig. 1(a), the screw of the pitch axis is

$$\$_{\mathrm{p}} = \{0,1,0;(0,0,H)\times(0,1,0)\}^{\mathrm{T}} = (0,1,0;-H,0,0)^{\mathrm{T}} \tag{23}$$

Due to the coplanarity of the limb axis and the pitch axis, hence

$$\begin{aligned}\$_{\mathrm{p}}\circ\$_{\mathrm{l}} &= -R\cos\theta[H + R_{\mathrm{P}}\sin(\alpha-\varphi)] + H[R\cos\theta - R_{\mathrm{P}}\cos(\alpha-\varphi)]\\ &= 0\end{aligned} \tag{24}$$

Furthermore, substituting Eq. (17) into Eq. (24) and simplifying, we arrive at

$$\begin{cases} R\cos\theta\sin[\alpha-\varphi(\theta)] + H\cos(\varphi(\theta)-\alpha) = 0\\ 0^\circ < \theta < 180^\circ\end{cases} \tag{25}$$

which is also a trigonometric equation with respect to θ in interval (0°, 180°), and its solution, denoted as θ_{b}, is the theoretical actuator

Table 3
Important theoretical and experimental actuator positions.

Position	Horizon (θ_{h})	Zenith (θ_{z})	Stiffness singularity (θ_{s})	Boundary singularity (θ_{b})	Cond (J)
Theoretical/(°)	142.41	99.34	94.90	25.48	7.2×10^6
Experimental/(°)	142.10	99.77	74.29	(28.13)	7.2×10^6

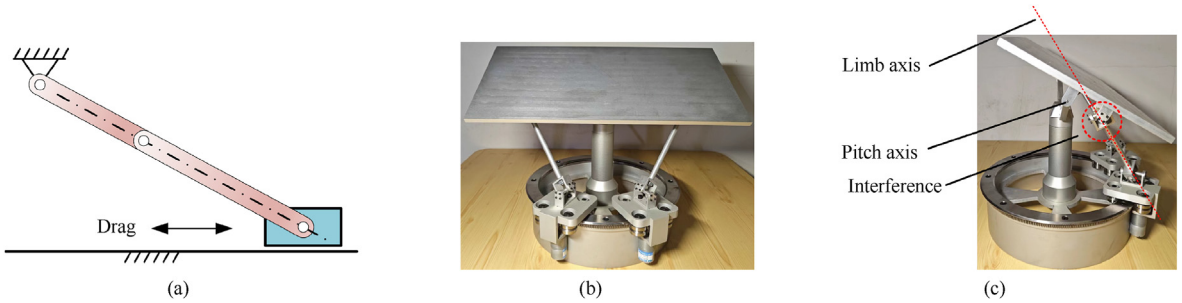

Fig. 14. Phenomenon of boundary singularity: (a) Boundary singularity of CSL-B; (b) Front view of configuration close to boundary singularity; (c) Side view of configuration close to boundary singularity.

position that produces the boundary singularity. As a summary, the important actuator positions, including both theoretically calculated and experimentally measured values, are listed out in Table 3, where the value in the brace "(•)" represents the actuator position closest to the boundary singularity, i.e., the actuator position in Figs. 14(b) and 4(c).

It can be seen from Table 3 that the theoretical values are considerably approximate to the experimentally measured values, indicating the reliability of both the theoretical methods and the prototype. It can also be concluded from Table 3 that there are no singularities in the TWS of the IAM, but there is a stiffness singularity outside the TWS, which is closest to the zenith configuration of the IAM. If the structural parameters of the IAM take on other values, the TWS is also singularity-free, which can also be illustrated by the CSL-B. As shown in Fig. 15(a), the crank is in the zenith position, the distance from the slider and the singularity, called singularity distance for the CSL-B, is d_s>0, the most common case. For the extreme case, the crank is also in the zenith position but the length of the coupler is reduced until it perpendicular to the slide, the singularity distance is d_s=0. Hence, the TWS supplied by the feasible solution of Eq. (10) or Eq. (17) is singularity-free according to the KMM.

According to Subsection 5.1, if the IAM is in the configuration of the stiffness singularity, it gains an additional DoF, resulting in zero stiffness. As a result, the closer the TWS of the IAM gets to this configuration, the lower its stiffness becomes. To guarantee a high stiffness of the IAM throughout the entire TWS, the concept of singularity distance (D_s) can also be defined for the IAM, similar to the singularity distance (d_s) concept of the CSL-B. According to the KMM, D_s can be defined as follows

$$D_s = \theta_z - \theta_s \tag{26}$$

The singularity distance D_s will serve as a constraint of the optimization problem in subsequent sections since it is an effective and important indicator to guarantee the stiffness of the IAM, which will be further demonstrated in Section 7.

6. Heuristic mechanism optimization

Given the motion characteristics of the CSL had been well studied over the past few centuries, the motion features of the CSL-B can be utilized as the guide for optimizing the IAM, according to the KMM. This section will employ a heuristic approach combined with the backtracking method to facilitate this process.

6.1. Optimization model

To reduce the IAM mass, the parameter H can be optimized in advance. In light of Fig. 1, the front cannot interfere with the base, during the pitch motion. Hence, in the horizon configuration, the below relation should be satisfied.

$$H > w + w_0 \tag{27}$$

By taking a value slightly greater than $w + w_0$ for H, not only is the mass reduced, but also the structural frequency is improved. This phenomenon arises because, with an identical cross-sectional area, a decreased column height leads to reduced mass and an increased fundamental frequency. The remaining parameters, d_1, d_2, w, and w_0 keep constant for simplicity since the base contributes

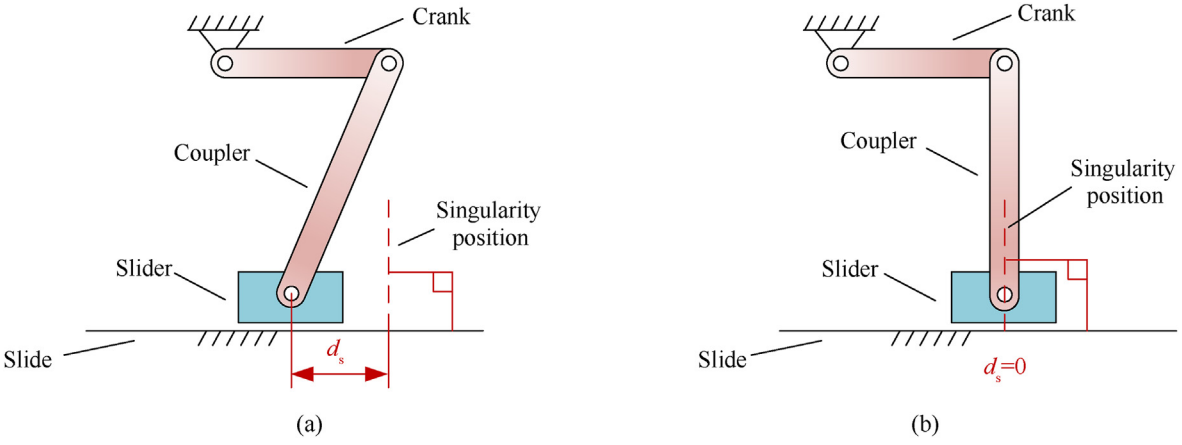

Fig. 15. Demonstration of singularity distance: (a) Case of $d_s > 0$; (b) Case of $d_s = 0$.

predominantly to the total mass of the IAM. As a result, in form, the mechanism optimization problem for reducing the IAM mass can be formulated as follows

$$\begin{cases} \text{find } (R,L)^{\mathrm{T}} \\ \min G(R,L) = 2\pi A_1 \rho R + 2A_2 \rho L + HA_3\rho \\ \text{s.t. } (R,L)^{\mathrm{T}} \in D_{\mathrm{f}} \end{cases} \tag{28}$$

where ρ is the material density of the prototype, G is the total mass of the base, limbs and column, as well as the meaning of A_1, A_2, A_3 can be found in Fig. 2(b) and Table 1. It is important to note that D_{f} represents the feasible region, which must ensure not only the TWS but also the specified singularity distance Λ_0. Furthermore, within these two constraints, it should also be guaranteed that there is no collision between the two actuators, as illustrated in Fig. 6. These constraints are highly complex and mutually coupled, making it challenging to formulating them explicitly in mathematical expressions.

6.2. Heuristic double backtracking algorithm

Directly solving the optimization problem in Eq. (28) poses challenges due to the implicit nature of D_{f}. As a result, for simplification of the optimization problem, the relevant constraints are decomposed into two parts, as shown in Fig. 16. The first part consists of two constraints: the TWS (equivalent to 0°–90° PAS) and the requirement of collision avoidance between the two actuators (equivalent to $I_{\mathrm{a}} \subset I_{\mathrm{b}}$ according to Eqs. (2) and (11)); the second part involves the requirement that the singularity distance must be greater than the prespecified threshold (i.e., $D_{\mathrm{s}} \geq \Lambda_0$). This treatment, if guided by the KMM, creates the favorable conditions for utilizing the backtracking procedure [58] an algorithm that is broad in its applicability and easy to implement. In this way, we can conduct the first backtracking to achieve the goals of the TWS and $I_{\mathrm{a}} \subset I_{\mathrm{b}}$. If $D_{\mathrm{s}} < \Lambda_0$ after the first backtracking, the second backtracking is implemented to achieve the remaining goal of $D_{\mathrm{s}} \geq \Lambda_0$, as illustrated in Fig. 16. All of the process will be implemented in a heuristic manner guided by the KMM, elaborated on below.

6.2.1. First backtracking

The goal of the first backtracking is to determine the appropriate values for R and L to achieve the 0°–90° PAS of the IAM. The principle to achieve this goal is illustrated in Fig. 17. In Fig. 17(a), the restricted stroke S_{r} of the slider is zero, resulting in the PAS having only one pitch angle ($\varphi_0 = \varphi_1$), which does not meet the requirement. In Fig. 17(b), increasing S_{r} to enlarge the PAS also fails to meet the requirement. Finally, in Fig. 17(c), S_{r} is further increased until it completely provides a 0°–90° PAS. According to the KMM, the corresponding operation for the IAM is constantly increasing the rail radius R from a small value until the 0°–90° PAS is achieved.

If suitable values for R and L yield the 0°–90° PAS, they must make the function 'arccos' sense in Eq. (10), indicating the necessity to confirm that the expression on the left-hand side of the below expression falls within the interval [-1, 1] exactly, wherein the left expression is redenoted as the right one for simplicity.

$$\frac{d_1^2 + H^2 + R_{\mathrm{p}}^2 + R^2 - L^2 - 2HR_{\mathrm{p}}\sin(\varphi - \alpha)}{2R\sqrt{d_1^2 + \left[R_{\mathrm{p}}\cos(\varphi - \alpha)\right]^2}} = \frac{T_1(\varphi) - L^2(\varphi)}{T_2(\varphi)} \tag{29}$$

Hence, for each φ in the interval [0°, 90°], the relation should be satisfied.

$$-1 \leq \frac{T_1(\varphi) - L^2(\varphi)}{T_2(\varphi)} \leq 1 \tag{30}$$

Consequently, we arrive at the inequality

$$\sqrt{T_1(\varphi) - T_2(\varphi)} \leq L(\varphi) \leq \sqrt{T_1(\varphi) + T_2(\varphi)} \tag{31}$$

and let

$$I(\varphi) = [T_1(\varphi) - T_2(\varphi), T_1(\varphi) + T_2(\varphi)] \tag{32}$$

Due to the 0°–90° PAS, the interval [0°, 90°] is sampled at $n+1$ points, denoted as $\varphi_0, \varphi_1, \cdots, \varphi_n$, where $\varphi_0 = 0°$ and $\varphi_0 = 90°$. This operation will produce $n+1$ intervals: $I(\varphi_0), I(\varphi_1), \cdots, I(\varphi_n)$, and their intersection I_l, which is a function of R, is defined as

$$I_l \triangleq \bigcap_{i=1}^{n} I(\varphi_i) \tag{33}$$

If $I_l \neq \varnothing$, it is redenoted as $[a_0, a_1]$. If the sampling points are sufficiently dense and I_l is not an empty set, then the pitch angle φ can completely traverse the interval [0°, 90°], indicating the achievement of the 0°–90° PAS of the IAM.

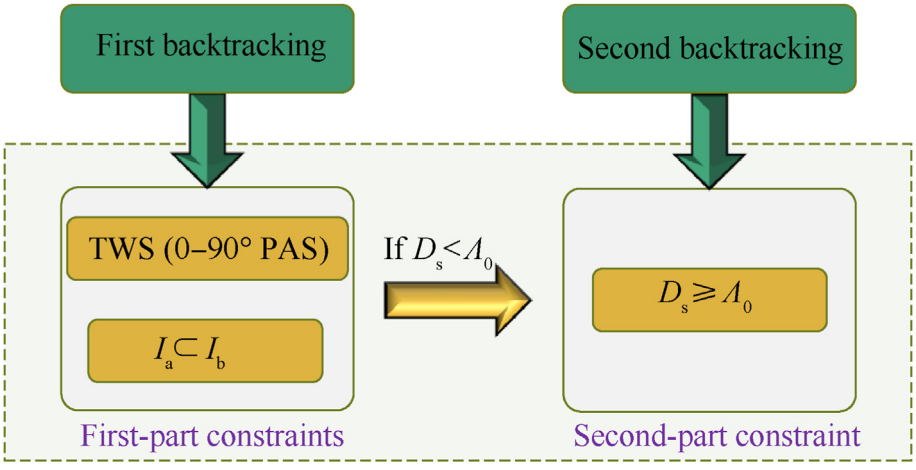

Fig. 16. Algorithm flowchart.

6.2.2. Second backtracking

The first backtracking ensures that the IAM maintains a pitch angle ranging from 0° to 90° without any collisions between actuators. However, it does not guarantee the magnitude of the singularity distance D_s, which quantifies the proximity of the TWS to the singularity. Therefore, a second backtracking is required to precisely control the singularity distance. The principle of controlling the singularity distance is illustrated by the CSL-B in Figs. 18 and 19. In Fig. 18(a), d_s is less than the prespecified threshold Λ_0, we can increase the d_s by simply increase the coupler length until it is greater than Λ_0, as shown in Fig. 18(b). According to the KMM, this operation is equivalent to the increase in limb length L to increase the singularity distance D_s for the IAM. As a result, there are two cases when the crank is in the horizon position, as shown in Fig. 19.

For the first case in Fig. 19(a), after the enlargement of the coupler length the slider is exactly contained in the limited stroke (S_r). According to the KMM, this phenomenon indicates that there is no collision between the two actuators of the IAM, namely, the increase in limb length is appropriate. However, for the case in Fig. 19(b), the slider exceeds the barrier, indicating that the two actuators collide with each other according to the KMM. This case can be avoided by simply increasing S_r, as shown in Fig. 19(c). Hence, from the KMM, this operation is equivalent to the increase in rail radius R to avoid the collision between the two actuators of the IAM.

6.3. Design of optimization algorithm

Ultimately, the two backtracking principles are implemented by the pseudocode presented in Algorithm 1, which is named as the heuristic double backtracking (HDB) algorithm. Thereinto, lines 1–8 are the implementation of the first backtracking to guarantee a singularity-free 0°–90° PAS, without any collision between the two actuators. Lines 9–20 implement the second backtracking to supply a large enough singularity distance D_s.

7. Results and discussion

This section begins with an illustration of the process and results of the HDB algorithm by an example. Parameters S_l, S_w, d, d_1, d_2, w and w_0, take the same values as those of the prototype, as shown in Table 1. According to Eq. (27), the height of the column can take H=100 mm as well as step lengths take h_1=2 mm, h_2=1 mm and h_3=1 mm, respectively. The number of sampled points is n=10, and they are $\varphi = 0°, 10°, \cdots, 90°$, respectively. The initial backtracking value of the rail radius is R_0=75 mm and the prespecified threshold for the singularity distance D_s is Λ_0=20°. All of the data are listed out in Table 4.

After execution of the HDB algorithm, the results are reported in Figs. 20 and 21 (values of R and L are rounded). It can be seen that the optimization process consists of two backtracking procedures. The first backtracking consists of 6 steps, and at the starting point R=75 mm, I_a is not contained in I_b; but as R increases to 85 mm, I_a is entirely enclosed within I_b. However, the singularity distance D_s=5.64° is less than the prespecified threshold Λ_0=20°. Hence, the second backtracking commences, comprising 5 steps with each step comprising 1 to 3 sub-steps. It can be seen that the final D_s is 20.75° greater than the prespecified Λ_0 and I_a is totally contained in I_b. Hence, all the constraints in Fig. 16 are met, the HDB algorithm terminates. In addition, in each step (including sub-steps), the singularity lies outside I_a, indicating that the singularity remains outside the TWS. This phenomenon verifies the claim made in Section 5 that the feasible solution of Eq. (10) or Eq. (17) is singularity-free within the TWS. The reduction in mass (ΔM) can be calculated using the following expression

$$\Delta M = \frac{\Delta R}{R} M_b + \frac{2\Delta L}{L} M_l + \frac{\Delta H}{H} M_c \tag{34}$$

where ΔR, ΔL and ΔH represent the reductions in rail radius, limb length and column height, respectively. The total volume (V_{blc})

Algorithm 1 Heuristic Double Backtracking (HDB)

Input: d, d_1, d_2, w, w_0, column height H, sampled points n, actuator dimensions S_l, S_w, threshold Λ_0, initial rail radius R_0, and step lengths h_1, h_2, h_3; The meaning of d, d_1 and d_2 is indicated Fig. 1.

1: $R \leftarrow R_0$;
2: Calculate I_l by Eq. (33), I_a by Eq. (11), and I_b by Eq. (2);
3: $L \leftarrow a_0$;
4: **while** $I_l \neq \varnothing$ **or** $I_a \not\subset I_b$ **do**
5: $R \leftarrow R + h_1$ First backtracking of R and L that supplies the 0°–90° PAS.
6: Calculate I_l, I_a, I_b;
7: $L \leftarrow a_0$;
8: **end while**
9: Calculate D_s by Eq. (26);
10: **while** $D_s < \Lambda_0$ **and** $I_a \not\subset I_b$ **do.** Second backtracking of R and L that supplies expected singularity distance D_s.
11: **while** $I_a \subset I_b$ **do**
12: $L \leftarrow L + h_2$
13: Calculate I_a, I_b and D_s;
14: **if** $D_s \geqslant \Lambda_0$ **then**
15: **break;**
16: **end if**
17: **end while**
18: $R \leftarrow R + h_3$
19: Calculate I_a, I_b;
20: **end while**
21: **return** R, L and D_s.

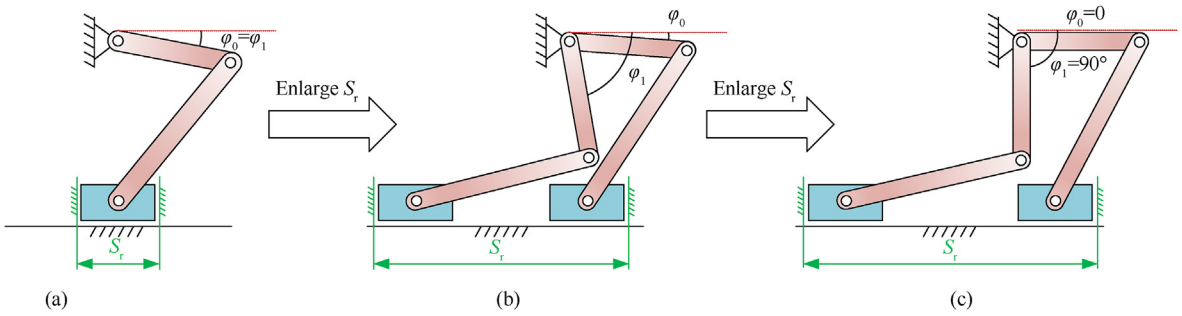

Fig. 17. Principle of first backtracking. φ_0 represents the initial pitch angle and φ_1 represents the end pitch angle.

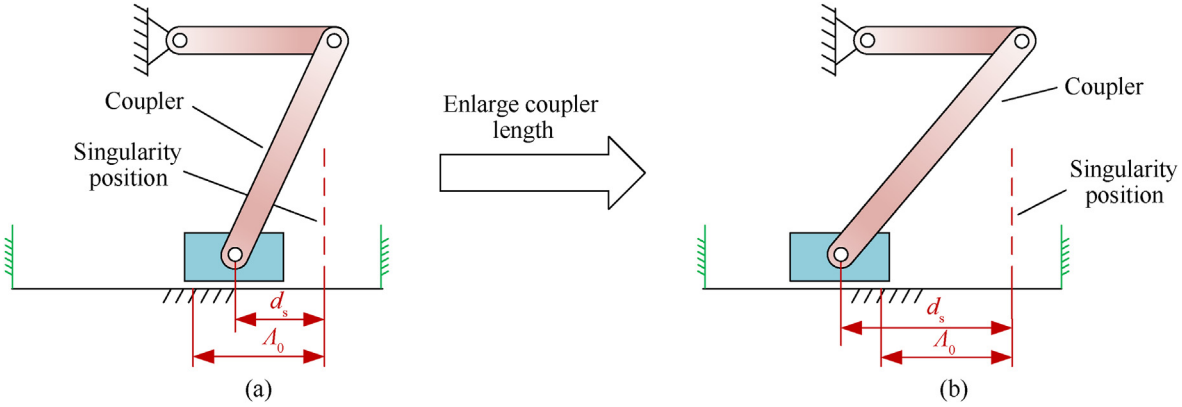

Fig. 18. Second backtracking - increasing singularity distance d_s: (a) d_s is not enough; (b) Increase d_s by increasing coupler length.

encompassing the base, the limbs and the column can be computed as

$$V_{\text{blc}} = 2\pi RA_1 + 2LA_2 + HA_3 \tag{35}$$

according to Fig. 2 and Table 1. Due to the materials are the same, V_{blc} can represent the total mass of the base, limbs and the column. As a result, the relations of R–Λ_0 and L–Λ_0 are shown in Fig. 22(a); the relation between Λ_0 and V_{blc} is shown in Fig. 22(b). In addition, the x-coordinates of the squared points (representing the prototype) is its corresponding D_s. These figures reflect the relations between the singularity distance D_s and the structural parameters (R, L and V_{blc}) indirectly since each prespecified Λ_0 is closely approximate to its corresponding D_s given by the HDB algorithm.

It can be seen from Fig. 22 that R, L and V_{blc} increase as Λ_0 increases, which indicates that the mass of the IAM increases with the increase in Λ_0. If Λ_0=20°, the reduction in R and L are 36.61 mm and 22.11 mm, respectively, while the reduction in V_{blc} compared to the prototype is 233.89 cm^3. If having the approximately identical singularity distance as the prototype (near Λ_0=24.5° in Fig. 22), the reductions in R, L and V_{blc} are 33.61 mm, 19.11 mm and 216.08 cm^3,

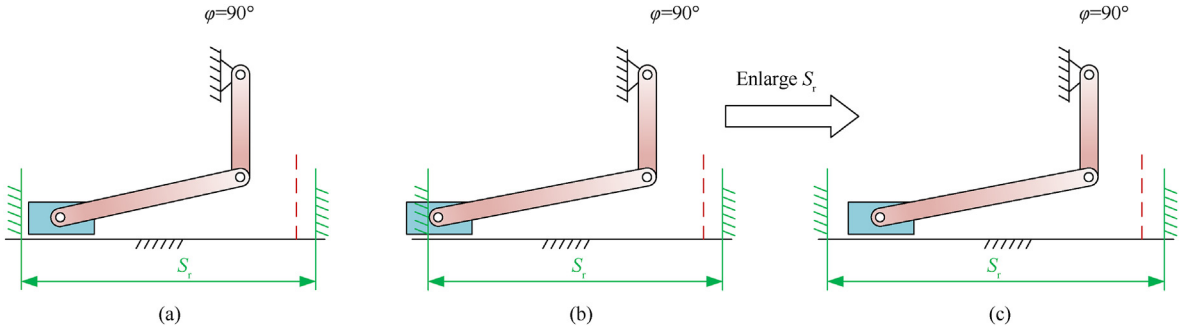

Fig. 19. Second backtracking - avoiding collision: (a) Case without collision; (b) Case with collision; (c) Theory of avoiding collision.

Table 4
Initial values of HDB algorithm.

S_1/mm	S_w/mm	d/mm	d_1/mm	d_2/mm	w/mm	w_0/mm	h/mm	h_1/mm	h_2/mm	h_3/mm	R_0/mm	n	Λ_0/(°)
75	75	9.4	127	204	39.72	60	100	2	1	1	75	10	20

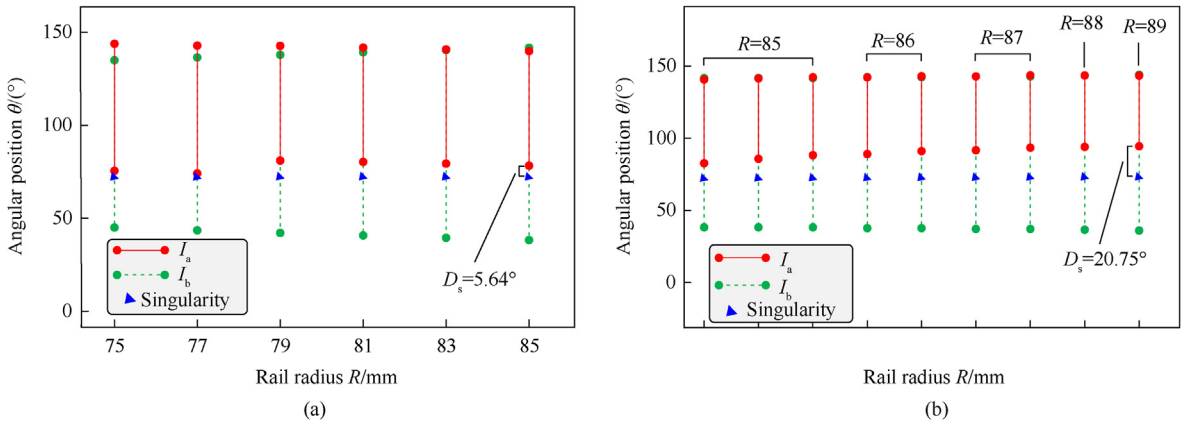

Fig. 20. Backtracking history of HDB algorithm-I: (a) First backtracking; (b) Second backtracking.

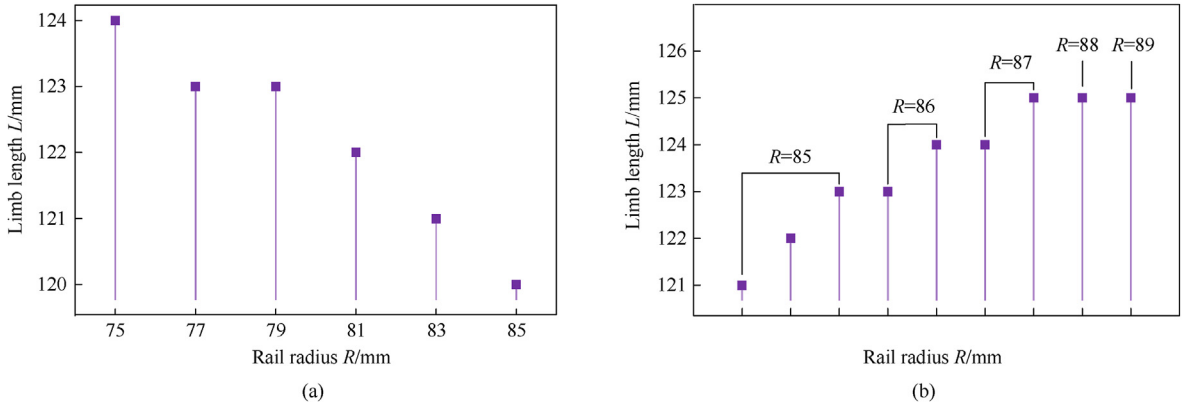

Fig. 21. Backtracking history of HDB algorithm-II: (a) First backtracking; (b) Second backtracking.

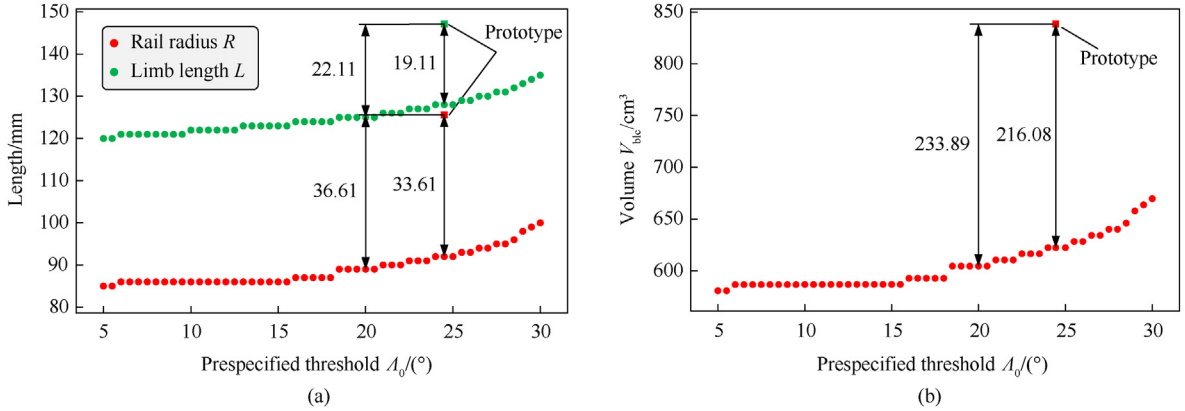

Fig. 22. Relations between Λ_0 and structural parameters: (a) Relations of R–Λ_0 and L–Λ_0; (b) Relation of V_{blc}–D_s.

respectively. The details before and after optimization by the HDB algorithm are reported in Tables 5 and 6. It can be seen from Table 5 that the mas M_{blc} deceases from 3.499 kg to 2.514 kg with an efficiency of 28%, and the total mass M of the IAM drops from 6.111 kg to 5.126 kg with an efficiency of 16%. Similarly, Table 6 indicates that the mass M_{blc} is reduced from 3.499 kg to 2.590 kg with an efficiency of 26%, and the total mass M of the IAM is reduced from 6.111 kg to 5.202 kg with an efficiency of 15%. These results demonstrate the substantial reduction in masses (M_{blc} and M) achievable using the HDB algorithm, indicating its effectiveness and superiority.

To explore the relation between the IAM's stiffness and the singularity distance D_s, the finite-element model (FEM) of the IAM is established by the ANSYS Parametric Design Language (APDL), as shown in Fig. 23(a). The modal analysis is performed and then the fundamental frequency f (first-order frequency) in the zenith configuration is extracted to characterize the stiffness of the IAM within the TWS, as shown in Fig. 23(b). For the red points in the figure, their corresponding Rs and Ls are obtained by the HDB algorithm using finer step lengths h_1=1 mm, h_2=0.02 mm,

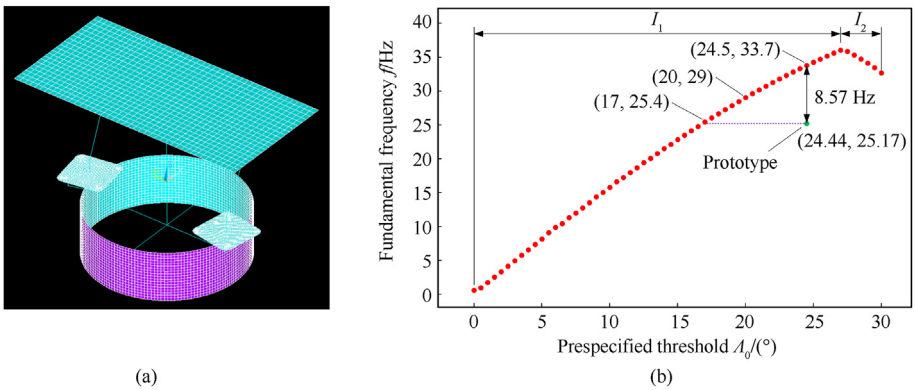

Fig. 23. Analysis of fundamental frequency: (a) Parametric FEM of IAM; (b) Fundamental frequency.

Table 5
Structural parameter values before and after optimization-I.

Parameter	H/mm	R/mm	L/mm	D_s/(°)	M_{blc}/kg	M/kg
Before	124.80	125.61	147.11	24.44	3.499	6.111
After	100	89	125	20.75(Λ_0=20)	2.514(28%)	5.126(16%)

h_3=0.02 mm.

It can be seen that when Λ_0=0, the fundamental frequency f approximately equals 0. This is because the corresponding singularity distance D_s is approximately 0, indicating that the TWS of the IAM is near the singular configuration. This phenomenon is totally in agreement with the intuition. Within interval I_1, frequency f increases as Λ_0 increases; but within interval I_2, f decreases with the increase in Λ_0. This phenomenon can be attributed to the common effect of two key factors. The first factor is configuration of the stiffness singularity, discussed in Subsection 5.1; the closer the IAM to this configuration the lower the stiffness. The second factor is the rail radius R and the limb length L, the larger they are, the lower the stiffness. In interval I_1, with the increase in Λ_0 from zero, the TWS gradually moves away from the singular configuration, which causes the increase in stiffness. On the other hand, as Λ_0 increases from zero, both R and L grow according to Fig. 22(a), resulting in reduced stiffness. Since the effect of the first factor is dominant over that of the second one, the overall tendency in interval I_1 presents an increase with the rise in Λ_0. However in I_2, since the effect of the second factor is dominant over that of the first one, the overall tendency of f in interval I_2 presents a decrease as Λ_0 increases. It is evident that the length of I_1 is much greater than that of I_2, hence it is necessary to maintain a sufficient D_s to achieve a high structural stiffness of the IAM.

It can also be observed that, even with the same Λ_0, the frequency f obtained by the HDB algorithm is greater than that of the prototype by about 8.57 Hz. This is because the lengths of R and L are reduced after the optimization by the HDB algorithm, according to Fig. 22(a) and Table 6. In addition, with the identical f as that of the prototype, the threshold set by the HDB algorithm is reduced from Λ_0=24.44° to Λ_0=17°, which implies that the mass of the IAM can be reduced further according to Fig. 22. All of the facts further demonstrate the superiority of the HDB algorithm.

The trend illustrated in Fig. 23(b) suggests that the singularity distance D_s is an effective stiffness indicator due to its positive correlation with the fundamental frequency f across a large interval (I_1) starting from 0. It is also indicated that D_s is an important (perhaps even the most important) indicator to evaluate the stiffness of the IAM within the TWS, because if D_s is fairly small, improving the IAM stiffness through structure optimization-increasing the cross-sectional areas of the constituent links of the IAM-have little or even no effect. As a result, improving the stiffness of the IAM should first concentrate on increasing the singularity distance D_s, followed by structural enhancement. One of the primary loads for ground-based phased array antennas is wind loading. Insufficient stiffness in the IAM can result in decreased antenna front accuracy under wind loading conditions, leading to a drastic deterioration in antenna electromagnetic (EM) performance, such as reduced gain and increased side lobe level. Therefore, the singularity distance D_s can play a significant role in improving antenna EM performance. These in-depth studies will be presented in our forthcoming work.

Fig. 22(b) also suggests that the mass will increase with the increase in Λ_0 (or D_s), hence, a larger singularity distance D_s is not necessarily better. In view of this fact, it is necessary to strike a balance between the mass of the IAM and its singularity distance. For instance, the IAM with Λ_0=20° is a good choice since it possesses a significant mass reduction and a favorable fundamental frequency of 29 Hz, according to Table 5 and Fig. 23(b). As a result, we choose the optimization results in Table 5 as the preferable and the 3D models before and after optimization are shown in Fig. 24. From the figure, it can be visually observed that the dimensions of the rail, limbs and column of the 3D model after optimization are reduced significantly. Also, the reduction in distance (colored in green bidirectional arrow) between the two actuators to the extent of potential interference indicates the full utilization of the circular rail. In addition, it is also observed in Fig. 25 that the 3D model after optimization can achieve a 0°–90° pitch motion and a 0°–360° azimuth motion, namely, the TWS is achieved. All of the facts demonstrate the effectiveness of the HDB algorithm further.

Guided by the KMM and the HDB algorithm, we are currently in the process of designing and fabricating our large-scale prototype. This prototype will serve as the platform for conducting extensive

Table 6
Structural parameter values before and after optimization-II.

Parameter	H/mm	R/mm	L/mm	D_s/(°)	M_{blc}/kg	M/kg
Before	124.80	125.61	147.11	24.44	3.499	6.111
After	100	92	128	25.12(Λ_0=24.44)	2.590(26%)	5.202(15%)

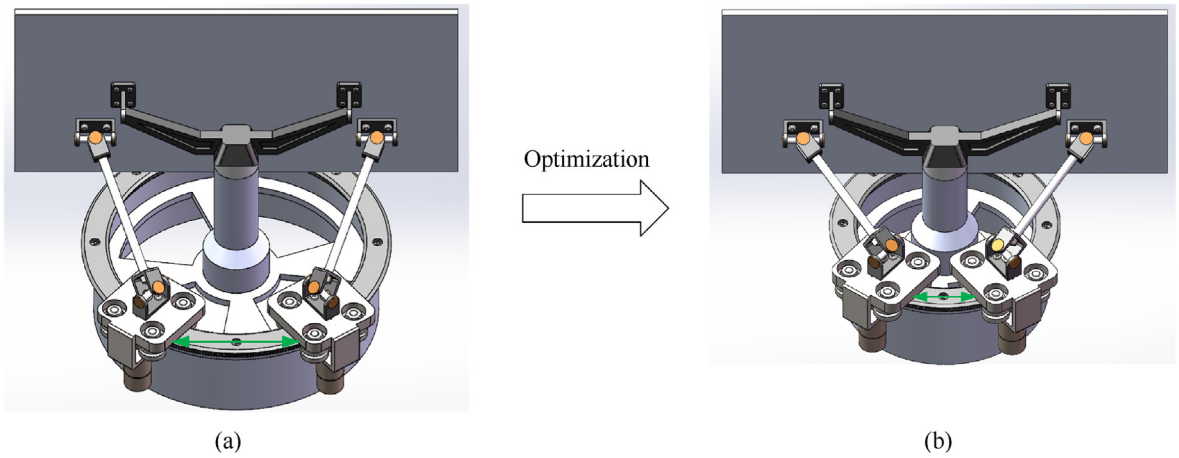

Fig. 24. 3D models before and after optimization: (a) Original 3D model; (b) 3D model after optimization.

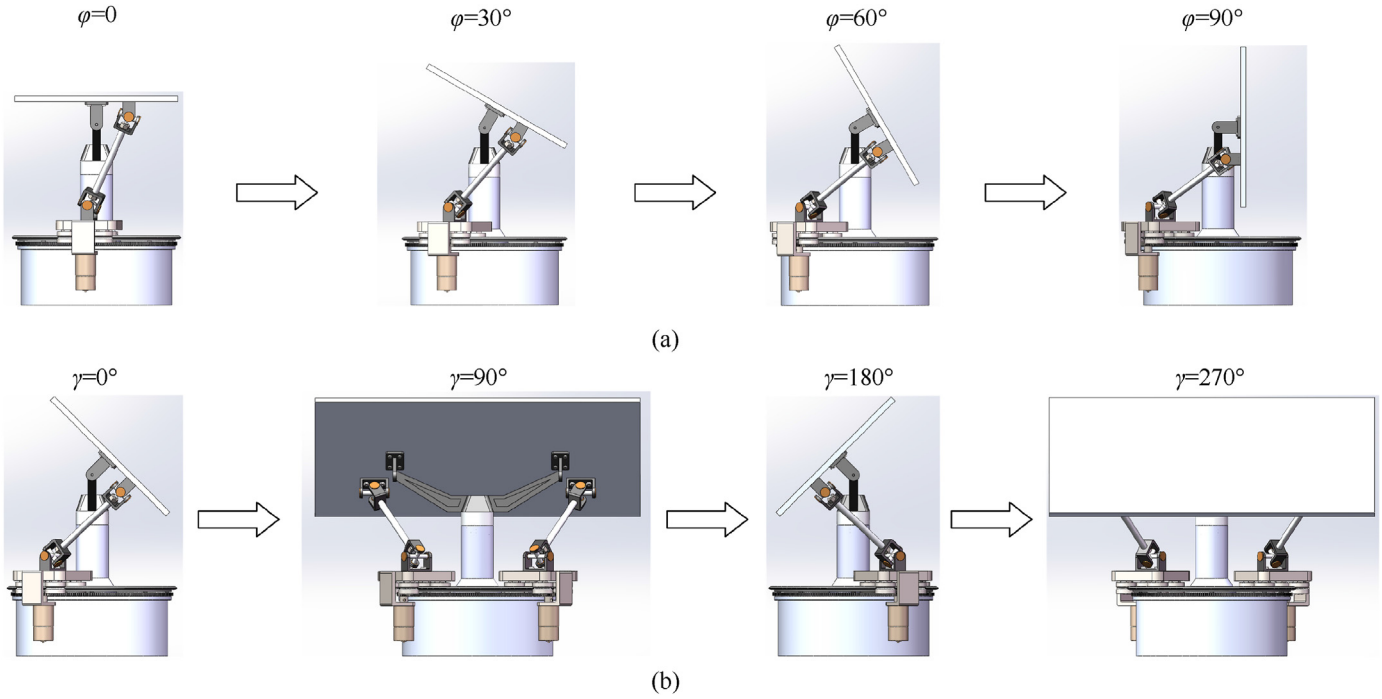

Fig. 25. Pitch motion and azimuth motion of 3D model after optimization: (a) Pitch motion (γ=0); (b) Azimuth motion ($\varphi = 45°$).

studies on structure optimization, motion/dynamical control, beam control, electromechanical coupling, and other related aspects. The findings and outcomes of these investigations will be comprehensively detailed in our forthcoming work. Our ultimate aim is to seamlessly integrate the proposed IAM into practical applications.

8. Conclusions

Aiming at analysis and optimization design of a 2-PSS&1-RR circular-rail parallel mechanism for fully steerable phased array antennas, this study presents several noteworthy innovations or contributions, summarized as follows

(1) The effectiveness of the innovative antenna mount (IAM) has been verified through a full-scale prototype, encompassing crucial aspects such as mechanism DoF, pitch motion, and azimuth motion.
(2) The kinematic mapping model (KMM) is an effective guiding framework for analyzing and optimizing the IAM, characterized by its concise and heuristic nature. Based on the KMM, the stiffness singularity is successfully identified, and hence the concept of singularity distance is introduced to evaluate the structural stiffness of the IAM. Furthermore, guided by the KMM, the novel HDB algorithm composed of two succinct backtracking procedures is developed, significantly reducing the total mass of the IAM (about 16%).
(3) The established parametric FEM of the IAM suggests a positive correlation between the fundamental frequency and the singularity distance across a broad range, starting from zero. This correlation suggests that the concept of singularity

distance can effectively reflect the structural stiffness of the IAM within the TWS. Consequently, it emerges as a promising technical indicator for designing this type of IAM.

Declaration of competing interest

The authors declare that they have no known competing financial interests or personal relationships that could have appeared to influence the work reported in this paper.

Acknowledgements

This work was financed by the National Key Research and Development Program of China, High efficiency space satellite charging system based on microwave wireless energy transfer technology (Grant No. 2021YFB3900304).

Appendix A. Supplementary data

Supplementary data to this article can be found online at https://doi.org/10.1016/j.dt.2024.03.001.

References

[1] Sun Z, Zhang Y, Yang D. Structural design, analysis, and experimental verification of an H-style deployable mechanism for large space-borne mesh antennas. Acta Astronaut 2021;178:481–98.
[2] Guo L, Zhao Y, Lu S. A novel spatial support mechanism for planar deployable antennas. Acta Astronaut 2021;188:479–90.
[3] Sun Z, Yang D, Duan B. Structural design, dynamic analysis, and verification test of a novel double-ring deployable truss for mesh antennas. Mech Mach Theor 2021;165:104416.
[4] Tan G, Duan X, Niu D. Visual synthesis of uniaxial synchronous deployment mechanisms for solid-surface deployable antennas. Mech Mach Theor 2022;178:105073.
[5] Chen Z, Shi C, Guo H. Design and accuracy analysis of a new high-rigidity modular planar deployable antenna mechanism. Eng Struct 2022;253:113770.
[6] Han B, Li X, Sun J. Design and dynamic analysis of a scissors hoop-rib truss deployable antenna mechanism. Defence Technology; 2023.
[7] Han B, Yuan Z, Hu X. Design and analysis of a hoop truss deployable antenna mechanism based on convex pentagon polyhedron unit. Mech Mach Theor 2023;186:105365.
[8] Guo L, Zhao Y, Chen B. Design of the connection mechanism between the basic units of a planar deployable antenna. Acta Astronaut 2023;202:462–75.
[9] Zhang Y, Gao C, Xu P. Type synthesis of deployable and symmetrical single-loop mechanisms for constructing aerospace platforms. Mech Mach Theor 2023;181:105212.
[10] Zhang Y, Xu P, Li B. Structure derivative design, network, and kinematic analysis of a class of two-dimensional deployable mechanisms for aerospace platforms. Mech Mach Theor 2023;185:105314.
[11] Shitov V. Evalution of the precision in setting a telescope with an alt-azimuth mounting. Meas Tech 1980;23:16–8.
[12] Dasgupta B, Mruthyunjaya T. The Stewart platform manipulator: a review. Mech Mach Theor 2000;35:15–40.
[13] Dunlop G, Ellis P, Afzulpurkar N. The satellite tracking keyhole problem: a parallel mechanism mount solution. Trans Inst Prof Eng N Z Electr Mech Chem Eng 1993;20:1–7.
[14] Kingsley J, Martin R, Gasho V. A Hexapod 12 m antenna design concept for the MMA, Technical Report. MMA Memo 1999;263.
[15] Deng X. Discussion about the Stewart platform mechanism for the application in the field of radar. Electro-Mechanical Engineering 2009;25:41–3 (in Chinese).
[16] Vuuren F. Design of a hexapod mount for a radio telescope. Stellenbosch: University of Stellenbosch; 2011. Ph.D. thesis.
[17] Duan Y, Jia Y, Li J. A configuration design of parallel mechanism applied to antenna mount. Machinery 2014;52:26–9 (in Chinese).
[18] Li B, Duan X, Mi J. Optimization design and trajectory planning of the parallel pedestal for multi-beam antenna. Electro-Mechanical Engineering 2018;34:14–23 (in Chinese).
[19] Sun Z, Liu J. The whole airspace tracking strategy based on 6-DOF parallel mechanism. Metrology & Measurement Technique 2023;50:53–6 (in Chinese).
[20] Reipurth B, Chini R, Lemke R. The VYSOS robotic telescope project. Astron Nachr 2004;325. 671-671.
[21] Chini R. The hexapod telescope-A never-ending story. In: Schielicke Reinhard E, editor. Reviews in modern astronomy 13: new astrophysical horizons, vol. 13. Hamburg, Germany: Astronomische Gesellschaft; 2000. p. 257–68. 2000., pp. 257–268.
[22] Koch P, Kesteven M, Nishioka H. The AMiBA hexapod telescope mount. Astrophys J 2009;694:1670.
[23] Dunlop G, Jones T. Position analysis of a 3-DOF parallel manipulator. Mech Mach Theor 1997;32:903–20.
[24] Dunlop G, Jones T. Position analysis of a two DOF parallel mechanism—the Canterbury tracker. Mech Mach Theor 1999;34:599–614.
[25] Dunlop G, Schlotter M, Hagedorn P. A singularity free parallel robotic mechanism for aiming antennas and cameras. Springer; 2006.
[26] Artemenko Y, Sil'vestrov E, Korenovskii V. Method for the synthesize of parallel-structure mechanisms for orientating a space telescope antenna. J Mach Manufact Reliab 2012;41:265–9.
[27] Yang Y, Zhou Z, Deng Y. Dynamics optimization and simulation of 3-RSR parallel Vehicle-borne antenna mechanisms. China Mech Eng 2019;30:1219.
[28] Zhang G, Guo J, Hou Y. Analysis of the PU-2UPS antenna parallel mechanism. J Mech Sci Technol 2021;35:717–28.
[29] Zhang G, Xia X, Hou Y. Optimal design and trajectory tracking experiment of a novel 3-DOF parallel antenna mechanism. AIP Adv 2022;12.
[30] Xu Y, Tong S, Wang B. Application of 2RPU-UPR parallel mechanism in antenna support. China Mech Eng 2019;30:1748 (in Chinese).
[31] Xu Y, Chen L, Yan W. Type synthesis of the hybrid rotary platform mechanism with three degrees of freedom. In: Mechanism and machine science: proceedings of ASIAN MMS 2016 & CCMMS 2016. Springer; 2017. p. 379–87.
[32] Xu Y, Ni S, Wang B. Design and calibration experiment of serial-parallel hybrid rotary platform with three degrees of freedom. In: Proceedings of the institution of mechanical engineers, Part C: journal of mechanical engineering science, vol. 233; 2019. p. 1807–17.
[33] Zhang G, Zheng D, Guo J. Dynamic modeling and mobility analysis of the 3-R (RRR) R+ R antenna mechanism. Robotica 2021;39:1485–503.
[34] Gosselin C, Hamel J. The agile eye: a high-performance three-degree-of-freedom camera-orienting device. In: Proceedings of the 1994 IEEE international conference on robotics and automation. IEEE; 1994. p. 781–6.
[35] Stanisic M, Wiitala J, Feix J. A dexterous humanoid shoulder mechanism. J Rob Syst 2001;18:737–45.
[36] Rosheim M, Sauter G. New high-angulation omnidirectional sensor mount. In: Free-space laser communication and laser imaging II, vol. 4821. SPIE; 2002. p. 163–74.
[37] Carricato M. Decoupled and homokinetic transmission of rotational motion via constant-velocity joints in closed- chain orientational manipulators. J Mech Robot 2009;4:041008.
[38] Ruggiu M. Kinematic and dynamic analysis of a two-degree-of-freedom spherical wrist. J Mech Robot 2010;2:031006.
[39] Guo W, Gao F, Deng Y. The new design of stabilised platform for target seekers using two-dof spherical linkage. Int J Des Eng 2010;3:337–54.
[40] Yu J, Wu K, Zong G. A comparative study on motion characteristics of three two-degree-of-freedom pointing mechanisms. J Mech Robot 2016;8:021027.
[41] Fomin A, Antonov A, Kiselev S. A new class of foldable mechanisms with a circular rail—FoldRail mechanisms. Mech Mach Theor 2023;189:105425.
[42] Rashoyan G, Lastochkin A, Glazunov V. Kinematic analysis of a spatial parallel structure mechanism with a circular guide. J Mach Manufact Reliab 2015;44:626–32.
[43] Fang H, Chen Z, Fang Y. A novel spherical parallel manipulator with circular guide. Appl Mech Mater 2013;325:1014–8.
[44] Li Q, Chen Q, Wu C. Two novel spherical 3-DOF parallel manipulators with circular prismatic pairs. In: International design Engineering technical conferences and computers and information in engineering conference, vol. 42568; 2006. p. 325–8.
[45] Kiselev S, Antonov A, Fomin A. Parallel robots with a circular guide: systematic review of kinematic schemes and methods of synthesis and analysis. J Mach Manufact Reliab 2022;51:20–9.
[46] Laryushkin P, Antonov A, Fomin A. Inverse and forward kinematics of a reconfigurable spherical parallel mechanism with a circular rail. In: Symposium on robot design, dynamics and control. Springer; 2022. p. 246–54.
[47] Laryushkin P, Antonov A, Fomin A. Novel reconfigurable spherical parallel mechanisms with a circular rail. Robotics 2022;11:30.
[48] Xu C, Xue C, Duan X. A novel 2R parallel mechanism for alt-azimuth pedestal. In: IOP conference series: materials science and engineering, vol. 428. IOP Publishing; 2018. p. 012053.
[49] Feng S, Duan X, Duan B. A novel design of large full-steerable reflector antenna. SCIENTIA SINICA Physica, Mechanica & Astronomica 2017;47:78–90 (in Chinese).
[50] Norton R. Design of machinery: an introduction to the synthesis and analysis of mechanisms and machines. McGraw-Hill Education; 2020.
[51] Merlet J. Jacobian, manipulability, condition number, and accuracy of parallel robots. J Mech Des 2006;132:199–206.
[52] Huang Z, Li Q, Ding H. Theory of parallel mechanisms, vol. 6. Springer Science & Business Media; 2012.
[53] Pei X, Yu J. A visual graphic approach for mobility analysis of parallel mechanisms. Front Mech Eng 2011;6:92–5.
[54] Yu J, Dong X, Pei X. Mobility and singularity analysis of a class of two degrees of freedom rotational parallel mechanisms using a visual graphic approach.

J Mech Robot 2012;4.
[55] Yu J, Pei X, Zong G. Graphical approach to creative design of mechanical devices. China Science Publishing & Media Ltd. (CSPM); 2014 (in Chinese).
[56] Liu X, Xie F, Wang J. Fundamental of parallel robotic mechanisms. Higher Education Press; 2018 (in Chinese).
[57] Zhang D, Gosselin C. Kinetostatic modeling of N-DOF parallel mechanisms with a passive constraining leg and prismatic actuators. J Mech Des 2001;123:375–81.
[58] Nocedal J, Wright S. Numerical optimization. Springer; 2006.